

# Depth Constraints on Azimuthal Anisotropy in the Great Basin from Rayleigh-wave Phase Velocity Maps<sup>☆</sup>

Caroline Beghein<sup>a,\*</sup>, J. Arthur Snoke<sup>b</sup>, Matthew J. Fouch<sup>c</sup>

<sup>a</sup>*University of California Los Angeles, Department of Earth and Space Sciences, 595 Charles Young Drive East, Box 951567, Los Angeles, CA 90095-1567, United States*

<sup>b</sup>*Department of Geosciences Virginia Polytechnic Institute and State University, 4044, Derring Hall (0420), Blacksburg, VA 24061, United States*

<sup>c</sup>*School of Earth and Space Exploration, Arizona State University, Bateman Physical Sciences Center F-wing, Tempe, AZ 85287, United States*

---

## Abstract

We present fundamental mode Rayleigh-wave azimuthally anisotropic phase velocity maps obtained for the Great Basin region at periods between 16 s and 102 s. These maps offer the first depth constraints on the origin of the semi-circular shear-wave splitting pattern observed in central Nevada, around a weak azimuthal anisotropy zone. A variety of explanations have been proposed to explain this signal, including an upwelling, toroidal mantle flow around a slab, lithospheric drip, and a megadetachment, but no consensus has been reached. Our phase velocity study help constrain the three-dimensional anisotropic structure of the upper mantle in this region and contribute to a better understanding of the deformation mechanisms taking place beneath the western United States. The dispersion measurements were made using data from the USArray Transportable Array. At

---

\*

*Email addresses:* [cbeghein@ucla.edu](mailto:cbeghein@ucla.edu) (Caroline Beghein)

<sup>1</sup>+1 310 825 0742

periods of 16 s and 18 s, which mostly sample the crust, we find a region of low anisotropy in central Nevada coinciding with locally reduced phase velocities, and surrounded by a semi-circular pattern of fast seismic directions. Away from central Nevada the fast directions are  $\sim$  N-S in the eastern Great Basin, NW-SE in the Walker Lane region, and they transition from E-W to N-S in the northwestern Great Basin. Our short period phase velocity maps, combined with recent crustal receiver function results, are consistent with the presence of a semi-circular anisotropy signal in the lithosphere in the vicinity of a locally thick crust. At longer periods (28-102 s), which sample the uppermost mantle, isotropic phase velocities are significantly reduced across the study region, and fast directions are more uniform with an  $\sim$  E-W fast axis. The transition in phase velocities and anisotropy can be attributed to the lithosphere-asthenosphere boundary at depths of  $\sim$  60 km. We interpret the fast seismic directions observed at longer periods in terms of present-day asthenospheric flow-driven deformation, possibly related to a combination of Juan de Fuca slab rollback and eastward-driven mantle flow from the Pacific asthenosphere. Our results also provide context to regional SKS splitting observations. We find that our short period phase velocity anisotropy can only explain  $\sim$  30% of the SKS splitting times, despite similar patterns in fast directions. This implies that the origin of the regional shear-wave splitting signal is complex and must also have a significant sublithospheric component.

*Key words:* Rayleigh-waves, Anisotropy, Lithosphere, Asthenosphere, Crust, USArray, Great Basin

---

## 1. Introduction

The Great Basin is located in the northern part of the Basin and Range Province in the western United States, and covers most of the state of Nevada, the southern part of Oregon, and the western part of Colorado (Figure 1). It is delimited to the west by the Sierra Nevada, to the north by the Snake River Plain, and to the east by the Colorado Plateau. The region is characterized by an average crustal thickness of about 30 km (Priestley et al., 1980; Catchings and Mooney, 1991; Zandt et al., 1995; Sheehan et al., 1997; Das and Nolet, 1998; Lerch et al., 2007) above a thin ( $\sim 30$  to 40 km) mantle lid (Burdick and Helmberger, 1978; Zandt et al., 1995). The presence of this thin lithosphere is probably the result of a large degree of lithospheric-scale extension (Hammond and Thatcher, 2004; Wernicke et al., 2008), but the details of lithospheric deformation constraints are not well known. In particular, the relationship between upper mantle processes and their surface tectonic signature is still rather poorly constrained in this region. Further, fundamental questions remain regarding the depth distribution of deformation and the interaction between the crust, the upper mantle lithosphere and the asthenosphere (Silver and Holt, 2002; Becker et al., 2006; Wernicke et al., 2008).

Seismic anisotropy, the dependence of seismic wave velocity with the direction of propagation or polarization of the wave, is a powerful tool that can give unique information about mantle deformation. In the crust it can result from the shape preferred orientation of fluid-filled cracks or lenses in responses to stress, and can be related to the presence of faults (Crampin et al., 1984). In the upper mantle, it is believed to be due to the lattice pre-

26 ferred orientation (LPO) of elastically anisotropic minerals, such as olivine.  
27 In the lithospheric mantle, the preferred alignment of olivine, or frozen-in  
28 anisotropy, is often attributed to deformation due to past tectonic processes  
29 (Karato and Toriumi, 1989; Ben-Ismaïl and Mainprice, 1998; Holtzman et al.,  
30 2003), while in the asthenosphere there is a general agreement that it is re-  
31 lated to present-day deformation (Nicolas et al., 1987; Smith et al., 2004;  
32 Marone and Romanowicz, 2007). The fast direction of wave propagation has  
33 been shown to be, in general, a good proxy for mantle flow when the flow is  
34 a progressive simple shear (Ribe, 1989; Becker et al., 2003). In some cases  
35 (presence of water or partial melt), however, the relation between shear direc-  
36 tion and seismic fast direction can be more complicated, making the interpre-  
37 tation of seismic anisotropy in terms of mantle deformation more challenging  
38 (Jung and Karato, 2001; Holtzman et al., 2003).

39 Shear-wave splitting constitutes a simple and relatively unambiguous  
40 manifestation of seismic anisotropy (Mitchell and Helmberger, 1973), and  
41 combined with geodynamic modeling it can provide information about man-  
42 tle deformation. In the western US, the interpretation of those results is,  
43 however, still controversial (Silver and Holt, 2002; Becker et al., 2006; Zandt  
44 and Humphreys, 2008; West et al., 2009). Specifically, shear-wave splitting  
45 studies show a semi-circular pattern of polarization directions surrounding a  
46 region of low splitting in central Nevada (Savage and Sheehan, 2000; West  
47 et al., 2009). The location of the anisotropy-low also coincides with a locally  
48 thick crust (Ozalaybey et al., 1997), a Bouguer gravity low (Simpson et al.,  
49 1986), and regionally reduced heat flow (Sass et al., 1994). The anisotropy  
50 pattern was initially interpreted as being caused by an upwelling (Savage and

51 Sheehan, 2000), and later as due to toroidal mantle flow around the edge of  
52 the Gorda-Juan de Fuca slab (Zandt and Humphreys, 2008). A more recent  
53 hypothesis is that of a lithospheric drip (West et al., 2009), based on the pres-  
54 ence of a high-velocity cylinder in the mantle beneath the Great Basin (Roth  
55 et al., 2008) combined with the lack of young volcanism and the presence of  
56 a local heat flow low. Decoupling between the crust and the mantle accom-  
57 panied by a megadetachment in the Great Basin was also recently proposed  
58 (Wernicke et al., 2008).

59 There is thus a variety of possible explanations for these shear-wave split-  
60 ting observations, and better depth constraints on the origin of the anisotropy  
61 signal are thus needed to improve our understanding of the deformation pro-  
62 cesses taking place beneath this region. One of the fundamental difficulties  
63 in interpreting shear-wave splitting data in terms of mantle deformation lies  
64 in the fact that analyses must be made using waves with nearly vertical inci-  
65 dence. shear-wave splitting therefore cannot provide constraints on the depth  
66 of origin or depth distribution of the azimuthal anisotropy. Surface waves  
67 and their dispersion properties are better suited for that purpose.

68 In this study we thus measured the dispersion of Rayleigh-wave funda-  
69 mental mode phase velocities over the period range 16 s to 170 s recorded  
70 from teleseisms on stations in the dense ( $\sim 70$  km spacing) USArray Trans-  
71 portable Array. We employed a traditional two-station method to determine  
72 inter-station phase velocities, which were then inverted to obtain azimuthally  
73 anisotropic phase velocity maps. The high density of seismic stations de-  
74 ployed in our study area enabled us to model azimuthal changes in Rayleigh-  
75 wave phase velocity with higher resolution than previously obtained for the

76 region. In addition, the use of surface waves allowed us, for the first time,  
77 to put some constraints on the depth of origin of the azimuthal anisotropy  
78 signal detected with shear-wave splitting in central Nevada. This will help  
79 shed light on the origin of the shear-wave splitting observations in the region.

## 80 **2. Data selection and preparation**

81 We analyzed vertical component seismograms for events recorded by the  
82 USArray Transportable Array (TA) broadband seismic stations. These sta-  
83 tions were deployed in Nevada starting in 2006 in the framework of the  
84 Earthscope project with an average station spacing of 70 km. We initially  
85 selected 59 teleseisms of minimum magnitude 5.0 and maximum depth of  
86 200 km, which occurred between October 2006 and October 2007 and for  
87 which Rayleigh-waves were recorded by the TA stations. Not all stations  
88 were in place during the entire period of this study, so the earliest events  
89 were recorded by fewer stations than those that occurred later on. We pro-  
90 cessed the seismograms for all the stations by correcting for the instrument  
91 response, decimating to 1 sample per second, and integrating to displace-  
92 ment.

93 For each earthquake, we then performed a frequency-time analysis (FTAN)  
94 (Dziewonski et al., 1969; Landisman et al., 1970) to identify the appropri-  
95 ate range of group velocities and to assess the quality of the group-velocity  
96 spectrum. Figure 2 shows examples of FTAN plots for vertical-component  
97 instrument-corrected waveforms at two stations along a common great-circle  
98 path from an event in our dataset. In both plots, the contours are smooth  
99 and well-behaved over periods that include the entire targeted period range.

100 We rejected stations and sometimes the event for which the FTAN plots dis-  
101 played irregularities. Such irregularities can be caused by small magnitude  
102 (leading to low signal-to-noise (S/N) ratio at the highest and lowest fre-  
103 quencies), complicated source function, paths that cross tectonic boundaries  
104 at sharp angles leading to multi-pathing, or frequency-dependent scattering  
105 from heterogeneities along the path (Deschamps et al., 2008a; Meier et al.,  
106 2004). Rejecting events or stations with irregular FTAN plots reduces pos-  
107 sible artifacts due to finite frequency effects.

### 108 **3. Rayleigh-wave phase velocity dispersion measurements**

109 The analysis procedure is a two-station method developed by Snoke and  
110 his colleagues, based on Herrmann’s developments (Herrmann, 1987) to de-  
111 termine inter-station dispersion phase velocities. This method has a long  
112 history (Sato, 1955; Knopoff, 1972) and enables measurements of phase ve-  
113 locities between two stations that share a common great-circle path with an  
114 event. This assumes that the deconvolution of the near-station waveform  
115 from the far-station waveform removes the effects on the calculated disper-  
116 sions of the structure between the epicenter and the near station. It has the  
117 advantage of reducing errors due to spectral anomalies that can be caused by  
118 the focal mechanism. For each earthquake, we thus identified and selected  
119 pairs of stations for which the difference (dbaz) between the backazimuths of  
120 the far station to the epicenter and to the near station was smaller than  $3^\circ$  to  
121 insure that the stations are aligned to a good approximation with a common  
122 great circle path. This restriction limits the number of usable events, but the  
123 dense network of TA stations enabled us to find many suitable station pairs

124 for a total of 28 teleseisms (Figure 3 and Table 1). Rayleigh-wave dispersion  
125 analyses were carried out for these 28 events.

126 We use a variant of the method developed by Herrmann (1987) to calcu-  
127 late estimates of interstation phase velocities and phase velocity errors from  
128 vertical-component waveforms for each identified station-pair. The method  
129 (see details in Warren et al. (2008)) uses coherencies and cross correlations  
130 for the two waveforms and calculates the full spectrum of the inter-station  
131 phase velocities in one step. The use of a reference phase-velocity spectrum  
132 calculated for a reference Earth model improves the coherence and typically  
133 removes the need for phase unwrapping. For the reference Earth model, we  
134 used a composite model, modified from the Tectonic North America (TNA)  
135 model (Grand and Helmberger, 1984), which is an upper mantle shear-wave-  
136 velocity model. We added the P-wave velocities and densities from model  
137 AK135 (Kennett et al., 1995), and the Catchings and Mooney (1991) Basin  
138 and Range crustal model. We call our reference model mTNA. The method  
139 provides a standard deviation estimate for the phase velocity at each fre-  
140 quency based on the coherency of the two waveforms after the near-station  
141 record has been time-shifted to the far-station time using the calculated phase  
142 velocities (Figure 4). A further data quality control was then performed by  
143 inspection of the power spectrum (Figure 4(B)). Station pairs for which the  
144 amplitude of the power spectrum decreased too fast were discarded. De-  
145 pending on the period, this leaves us with between 600 and 850 station pair  
146 paths.

## 147 4. Azimuthally anisotropic phase velocity maps

### 148 4.1. Inversion of the path-averaged measurements

The measurements  $\bar{c}$  performed with the two-station method are averages of the phase velocity  $c$  calculated along the great circle path that connects the two stations considered :

$$\bar{c}(T) = \int_{\Delta_1}^{\Delta_2} c(T, l) dl \quad (1)$$

149 where  $T$  is the period of the wave, and  $l$  designates the great circle path  
150 between stations 1 and 2 at epicentral distance  $\Delta_1$  and  $\Delta_2$ , respectively.  
151 We constructed phase velocity maps by inversion of equation 1 using the  
152 LSQR (Paige and Saunders, 1982) inversion procedure described by Lebedev  
153 and van der Hilst (2008). Uncertainties on the phase velocity maps at a  
154 given period are estimated using an average of the uncertainties on the path-  
155 averaged measurements.

The LSQR method employed allows us to model changes in the phase velocity with the azimuth of propagation, and thus determine estimates for seismic azimuthal anisotropy if the backazimuths of our stations cover a range of at least  $90^\circ$ , which is the case for our data set. In a slightly anisotropic medium, the phase velocity can be expressed as a function of the horizontal direction of propagation (azimuth  $\Psi$ ) as follows (Smith and Dahlen, 1973) :

$$c(T, \Psi) = c_0(T) + c_1(T)\cos(2\Psi) + c_2(T)\sin(2\Psi) + c_3(T)\cos(4\Psi) + c_4(T)\sin(4\Psi) \quad (2)$$

where  $T$  represents the period of the wave.  $c_0$  is the isotropic (averaged over all azimuths) part of the phase velocity and the other terms describe the

azimuthal dependence of the phase velocity. This equation can be written as :

$$\mathbf{d} = \mathbf{G}\mathbf{m} \quad (3)$$

where  $\mathbf{m}$  is the vector representing the model parameters ( $c_0$ ,  $c_1$ ,  $c_2$ ,  $c_3$  and  $c_4$  in equation 2),  $\mathbf{d}$  is the data vector, and  $\mathbf{G}$  is the matrix describing the physical relationship between observations and model parameters. The directions of fast propagation  $\Theta_{2\Psi}$  and  $\Theta_{4\Psi}$  are obtained by calculating :

$$\Theta_{2\Psi} = \frac{1}{2} \arctan\left(\frac{c_2}{c_1}\right) \quad (4)$$

$$\Theta_{4\Psi} = \frac{1}{2} \arctan\left(\frac{c_4}{c_3}\right) \quad (5)$$

and the amplitudes of the anisotropy is given by :

$$\Lambda_{2\Psi} = \sqrt{c_2^2 + c_1^2} \quad (6)$$

$$\Lambda_{4\Psi} = \sqrt{c_4^2 + c_3^2} \quad (7)$$

156 Our data yielded sufficient azimuthal coverage to enable us to estimate  
 157 the azimuthal dependence of the phase velocities across the Great Basin.  
 158 We introduced these anisotropic terms in the inversions of the path-averaged  
 159 phase velocity measurements with a moderate amount of lateral smoothing,  
 160 and we tested different sized triangular model grids. The choice of the grid  
 161 spacing is subjective, but should remain smaller than the target resolution,  
 162 which itself is dependent on the station spacing and the azimuthal coverage  
 163 achieved. A grid spacing that is too large is equivalent to applying too  
 164 much smoothing and we would be unable to see potentially interesting model  
 165 features. A grid spacing too small could display small scale variations, which  
 166 may not be resolvable. We performed tests using 30, 45, and 60 km. The

167 results presented in section 5 were made using a 45 km grid. Maps obtained  
 168 with a 30 km grid spacing gave results similar to those presented here but  
 169 with smaller scale variations, which cannot confidently be resolved. Maps  
 170 obtained with a 60 km spacing were similar to those shown here, only slightly  
 171 smoother.

172 *4.2. Significance of the anisotropy*

We found that including the azimuthal terms in the inversion of equation 2 decreases the total variance compared to inversions including only the  $0\Psi$  terms ( $c_0$  in equation 2). However, this decrease could be due to an increase in the total number of unknowns and not necessarily be required by the data. In order to insure that the anisotropy introduced was statistically significant we adopted the method described by Trampert and Woodhouse (2003). it uses a reduced  $\chi^2$  defined as :

$$\chi^2 = \frac{1}{N - M}(\mathbf{d} - \mathbf{G}\mathbf{m})\mathbf{C}_d^{-1}(\mathbf{d} - \mathbf{G}\mathbf{m}) \quad (8)$$

where  $C_d$  is the data covariance matrix,  $N$  is the total number of data, and  $M$  is the trace of the resolution matrix  $\mathbf{R}$ . The resolution matrix cannot be directly obtained from the LSQR method, but it can be calculated by inverting each column  $j$  of matrix  $\mathbf{G}$  (Trampert and L ev eque, 1990). If  $\mathbf{G}_j$  is the vector formed by the  $j^{th}$  column of  $\mathbf{G}$  we can solve :

$$\mathbf{R}_j = \mathbf{L}\mathbf{G}_j \quad (9)$$

173 where  $\mathbf{L}$  represents the LSQR operator.  $\mathbf{R}_j$  is then column  $j$  of the resolution  
 174 matrix. The trace of the resolution matrix increases as the applied damping  
 175 decreases, and  $\chi^2$  decreases (Figure 5). In order to test whether a decrease

176 in  $\chi^2$  between two inversions is significant, we performed a standard F-test  
177 based on the number of free parameters  $N - M$  used to construct the models,  
178 following Trampert and Woodhouse (2003). Note that here, because the  
179 total number of data is the same in each inversion, comparing models based  
180 directly on the trace of  $\mathbf{R}$  is equivalent to comparing them based on the  
181 number of independent variables.

182 Extensive tests showed that including the  $2\Psi$  terms in equation 2 signifi-  
183 cantly improved the data fit compared to inversions with the  $0\Psi$  terms only,  
184 and adding the  $4\Psi$  terms significantly reduced the  $\chi^2$  misfit furthermore. An  
185 example is given in Figure 5 for measurements made at 38 s period and  
186 shows that, for a given number of independent parameters,  $\chi^2$  was lowered  
187 as the different anisotropy terms were added to the inversions. The F-tests  
188 determined that these changes in reduced  $\chi^2$  are statistically significant :  
189 For instance, we calculated that there is a 92% probability that the reduc-  
190 tion in misfit between our "preferred"  $0\Psi + 2\Psi$  inversion and our "preferred"  
191  $0\Psi + 2\Psi + 4\Psi$  inversion is significant. Similar results were found at all periods  
192 measured between 16 s and 102 s. We can therefore conclude that the data  
193 we collected for these periods require the presence of azimuthal anisotropy  
194 to explain the measured phase velocities.

### 195 *4.3. Finite Frequency Effects*

196 The two station method employed here is based on ray theory: it thus  
197 assumes that off-great circle path scattering is negligible and that the decon-  
198 volution of the near-station waveform from the far-station waveform removes  
199 the effects of structure between the epicenter and the near station. However,  
200 due to their finite frequencies, surface waves are sensitive to structure outside

201 of the great circle path, and the measurements can be affected by diffraction  
202 and wavefront interference. Perturbations due to lateral heterogeneities near  
203 the great circle path can be accounted for by using 2-D sensitivity kernels  
204 (Zhou et al., 2005). The method we employed to generate phase velocity  
205 maps from our path-averaged measurements uses a finite width approxima-  
206 tion of along-path sensitivity kernels (Lebedev and van der Hilst, 2008).

207 Whether accounting for finite frequency effects significantly improves the  
208 final tomographic models has been vigorously debated over the past few years  
209 (van der Hilst and de Hoop, 2005; Yang and Forsyth, 2006; Sieminski et al.,  
210 2004; Trampert and Spetzler, 2006). It has been argued that equivalent  
211 tomographic models can be obtained with ray or finite frequency theory as  
212 long as adequate regularization is chosen (Sieminski et al., 2004). The reason  
213 invoked is that the advantages of accounting for finite frequency effects are  
214 lost in the null-space when path coverage is not perfect, which is most often  
215 the case for the Earth (Trampert and Spetzler, 2006). In this study, we  
216 already removed potential scattering artifacts at the FTAN analysis stage  
217 by discarding events and/or stations with irregular group velocity plots. We  
218 tested whether any remaining finite frequency effects were influencing our  
219 results by choosing kernels of varying widths and comparing the calculated  
220 phase-velocity maps with those calculated using ray theory. We did not find  
221 significant differences in the results.

## 222 **5. Results**

223 Phase velocity maps were obtained from the path-averaged phase velocity  
224 measurements made at periods of 16, 18, 20, 22, 25, 28, 33, 38, 44, 54, 68,

225 85, 102 s. Note that we also analyzed longer period (128 s and 170 s) data,  
226 but do not include the corresponding phase velocity maps here because they  
227 required strong lateral smoothing and the amplitudes of the final models  
228 were very low. We concluded that our measurements are unable to constrain  
229 lateral variations in phase velocities with respect to mTNA at these higher  
230 periods. The azimuthally anisotropic phase velocity maps obtained between  
231 16 s and 102 s are presented in Figure 6. The corresponding ray coverage is  
232 shown in Figure 7. Changes in the isotropic part of the phase velocity maps  
233 with respect to mTNA were found with peak amplitudes of approximately  
234 2-4 %, as detailed below.

235 Figure 8 shows the sensitivity kernels, or partial derivatives, of the fundamental-  
236 mode phase velocities with respect to  $V_S$  based on velocity model mTNA.  
237 It shows that data analyzed between 16 s and 20 s period mostly sample  
238 the top 30 km of the Great Basin, which corresponds to the average crustal  
239 thickness for the region. Between 22 s and about 28 s, the phase velocity  
240 maps obtained average structure in the top  $\simeq 60$  km, i.e., in the crust and  
241 the upper mantle lithosphere, and longer period data sample part of the  
242 lithosphere and the upper asthenosphere.

243 Our results (Figure 6) show that lateral changes in the isotropic phase  
244 velocities are present at short periods (from 16 to 25 s), but they tend to fade  
245 at longer periods. Between 28 s and 68 s period, the isotropic phase velocities  
246 are much more uniform over the Great Basin, with values lower than the  
247 phase velocity predicted by mTNA. At 85 s and 102 s, the northern part  
248 of the region appears to be characterized by phase velocities slightly larger  
249 than those predicted by mTNA. Making a fair and quantitative comparison

250 of our phase velocity maps with maps produced by other groups (Pollitz,  
251 2008; Yang et al., 2008) is not straightforward because of different choices of  
252 measurements and inversion techniques, data selection, etc (Trampert, 1998).  
253 However, we observed a similarity between our low period (16 s and 18 s)  
254 maps with the 16 s map obtained with ambient noise tomography (Yang  
255 et al., 2008) : In both cases, there is reduction in phase velocity in south  
256 central Nevada. In addition, both sets of short period maps show a lower  
257 phase velocity region in the northwest corner of the Great Basin, despite the  
258 fact that in our case this corresponds to the edge of our model where data  
259 coverage is low. The clear reduction in phase velocity across the region found  
260 between 28 s and 68 s is consistent with phase velocities in the High Lava  
261 Plains, northwest of our study region (Warren et al., 2008).

262 At most periods, the isotropic phase velocities did not significantly de-  
263 pend on whether azimuthal anisotropy was included in the inversions. The  
264 exception was found for data measured at 85 s. In that case, the back-  
265 ground phase velocity changed quite significantly with the introduction of  
266 anisotropy, but mostly at the edges of our study region, where ray coverage  
267 is sparse. This is indicative of the presence of trade-offs between the  $0\Psi$ ,  $2\Psi$ ,  
268 and  $4\Psi$  terms of equation 2. We note, however, that the 85 s map obtained  
269 without including the anisotropic terms was significantly different from the  
270 maps obtained at 68 s and 102 s, but it became similar to the one obtained  
271 at 102 s when we added the anisotropic terms. This, in addition to the F-test  
272 results discussed in section 4.2, gives us confidence that azimuthal anisotropy  
273 is required to explain our measurements.

274 At most periods, the modeled  $2\Psi$  anisotropy has mean and peak ampli-

275 tudes varying approximately between 1 % and 2 % and 2 % and 5 %, respec-  
276 tively (Figure 9). These amplitudes should, of course, not be taken at face  
277 value since they are affected by the damping and the strongest values tend to  
278 be found near the edges of the study region where ray coverage is less dense.  
279 Given these caveats, it appears that anisotropy beneath the Great Basin is  
280 relatively strong at the shortest periods (16 s - 18 s), decreases between 22 s  
281 and 68 s, and then increases at longer periods (85 s and 102 s).

282 Figure 6 also reveals very interesting patterns of azimuthal anisotropy.  
283 At short periods (16 s and 18 s), we observe a semi-circular pattern of fast  
284 seismic directions surrounding a small region (about 200 km wide) of low  
285 azimuthal anisotropy centered near  $243^\circ$  longitude and  $39^\circ$  latitude. This  
286 peculiar pattern is similar (but not identical) to the shear-wave splitting  
287 pattern found in previous studies in the region (Savage and Sheehan, 2000;  
288 West et al., 2009). Interestingly, the location of the zone of low-to-zero  
289 azimuthal anisotropy found at short periods is also the location of a reduction  
290 in phase velocity with respect to the mTNA prediction. The fast direction  
291 of propagation thus appears to rotate around the negative phase velocity  
292 anomaly. As the period increases, the lower phase velocity region becomes  
293 progressively wider and the anisotropy pattern changes. The low-to-null  
294 azimuthal anisotropy region is no longer visible, but the anisotropy pattern  
295 remains rather complicated. At 44 s and longer periods, the fast direction  
296 in the southern Great Basin is approximately SE-NW, while in the northern  
297 part (roughly at the location of the positive phase velocity anomaly visible  
298 at 85 s and 102 s) it appears oriented in a more SW-NE direction.

299 Figure 10 displays synthetic tests performed to determine whether the

300 patterns seen in our models can be resolved with our data. The first input  
301 model is the outcome of the real data inversion at 18 s, with a zone of no  
302 azimuthal anisotropy surrounded by a semi-circular pattern (Figure 10 (A)).  
303 We inverted the corresponding synthetic data using the same inter-station  
304 paths as the ones employed for the 18 s inversions. We see that the anisotropic  
305 amplitudes are slightly lower after inversion due to the regularization, but the  
306 isotropic amplitudes are relatively well recovered (Figure 10 (B)). In addition,  
307 the input anisotropy pattern is well recovered, which gives us confidence that  
308 the anomalous region is resolved by our shortest period data and not an  
309 artifact of the inversion scheme. We also performed synthetic tests at 44 s.  
310 The anisotropy in model C is identical to that of model A but the phase  
311 velocity is assumed to be uniform. The test shows that the amplitude of  
312 the isotropic part of the model is relatively well recovered (Figure 10 (D)).  
313 The azimuthal anisotropy "hole" is, however, not resolved and the anisotropy  
314 in the output model is more uniform. Input model E is identical to input  
315 model C, except for a positive phase velocity anomaly that we associate  
316 with the region of reduced azimuthal anisotropy. A similar phase velocity  
317 map can be expected from the lithospheric drip model proposed by West  
318 et al. (2009), where a lithospheric drip induces strong mantle downwelling  
319 and locally eliminates azimuthal anisotropy. In output model F, we see that  
320 neither the semi-circular anisotropy pattern nor the positive anomaly can be  
321 recovered at those periods. This is due to the fact that lateral resolution  
322 is not only limited by path coverage and station spacing, but also by the  
323 wavelength of the waves analyzed. In this case, the phase velocity of a 44 s  
324 Rayleigh-wave is about 3.7 km/s (Figure 6), corresponding to a wavelength

325 of approximately 160 km, to be compared with a synthetic anomaly with a  
326 200 km width. Improvements in lateral resolution at those periods may be  
327 obtained in future studies with a more exact application of finite frequency  
328 theory than the approximation we employed here (Lebedev and van der Hilst,  
329 2008).

## 330 **6. Discussion**

### 331 *6.1. Isotropic phase velocities across the Great Basin*

332 Between periods of 16 s and 25 s, which sample the thin Great Basin  
333 lithosphere, our models are characterized by lateral changes in phase velocity.  
334 The local reduction in phase velocity seen at 16 s and 18 s (mostly sensitive  
335 to crustal depths) in south central Nevada could be due to lateral changes  
336 in composition, or (though less likely) changes in temperature. However,  
337 a more likely interpretation is that our results document the presence of a  
338 locally deeper Moho, consistent with regional receiver function constraints  
339 (Ozalaybey et al., 1997; Crotwell and Owens, 2005). To determine the effect  
340 of a change in the Moho depth on short-period phase velocities, we used  
341 our forward-modeling code (Herrmann, 1987) for the mTNA velocity model  
342 with an increase of 5 km in crustal thickness. This change reduces the phase  
343 velocity at 16 s by about 0.7%, which is consistent with the magnitude of  
344 the phase velocity reduction seen in our model at 16 s period.

345 Between periods of 28 s and 68 s, Rayleigh-waves are primarily sensitive  
346 to depths between 20 km and 150 km, but have peak sensitivity between  
347 about 40 km and 80 km. These periods therefore sample the lower part of  
348 the mantle lithosphere and the upper asthenosphere. Our results show that

349 the isotropic phase velocities at those periods are generally more uniform  
350 and lower by about 3% than those predicted by mTNA. This suggests that  
351 the lithosphere is quite thin beneath the Great Basin, perhaps as thin as  
352 50-60 km, in agreement with results by Burdick and Helmberger (1978) and  
353 Zandt et al. (1995). Furthermore, the reduced phase velocities at these longer  
354 periods provide strong evidence for a warmer asthenospheric mantle than one  
355 would conclude based on model mTNA. This result is also consistent with the  
356 regionally high heat flow observed across the region (Sass et al., 1994) and  
357 may help explain the regional Bouguer gravity low (Simpson et al., 1986).  
358 Our models also suggest that the top of the increased velocity cylinder imaged  
359 by body wave tomography (Roth et al., 2008) may be located at about 75 km  
360 depth or perhaps slightly deeper. This finding implies that, if the lithospheric  
361 drip hypothesis of West et al. (2009) is correct, the drip process may be in  
362 its final stages of detaching from the overlying lithospheric plate. We also  
363 note that the location of the positive phase velocity anomaly observed at 85  
364 and 102 s in the northern Great Basin could correspond to the southern edge  
365 of the Juan de Fuca slab imaged in P-wave tomography studies (Roth et al.,  
366 2008; Sigloch et al., 2008; Burdick et al., 2008; West et al., 2009). Depth  
367 inversions of the phase velocity maps are being performed in ongoing work,  
368 which will enable us to determine the amplitude of this reduction in velocity,  
369 and inferentially temperature, at depth.

## 370 *6.2. Azimuthal anisotropy*

371 Our results demonstrate that seismic azimuthal anisotropy is present over  
372 most depths of the crust and uppermost mantle, suggesting that deforma-  
373 tion extends to significant depth beneath the Great Basin. This finding

374 is in general agreement with previous, larger-scale studies, which detected  
375 seismic anisotropy over most of the western US in the crust (Bensen et al.,  
376 2008), and in the mantle to depths of at least 200-300 km (Hearn, 1996;  
377 Marone and Romanowicz, 2007; Nettles and Dziewonski, 2008). This result  
378 also generally agrees with Beghoul and Barazangi (1990) who reported the  
379 presence of about 3.2% variations in seismic wave velocity with the azimuth  
380 of propagation in the Great Basin from  $P_n$  travel time measurements.

381 At short periods (16 s and 18 s), our models are characterized by a  
382 semi-circular fast seismic direction surrounding a zone of lower phase veloc-  
383 ity and low-to-null azimuthal anisotropy, similar to shear-wave splitting fast  
384 polarization directions. At longer periods, the fast direction pattern is gen-  
385 erally more homogeneous, apart from a slight change in fast direction in the  
386 northwestern Great Basin. This change in fast direction is more strongly  
387 visible at 85 s and 102 s, where it coincides with a lateral change in phase  
388 velocity with respect to mTNA predictions. Considering the depth sensi-  
389 tivity of our data (Figure 8), our results suggest that the semi-circular fast  
390 direction observed at short periods is of lithospheric origin, and varies over  
391 scales of  $\sim 50$  km. The transition between a complex anisotropy pattern  
392 at short periods and a more homogeneous fast direction at longer periods  
393 is thus compatible with a two-layer model of azimuthal anisotropy (Marone  
394 and Romanowicz, 2007; Deschamps et al., 2008b). In this model, the upper  
395 layer anisotropy is attributed to a "frozen-in" manifestation of past deforma-  
396 tion mechanisms associated with tectonic events, while the lower layer fast  
397 direction reflects current mantle deformation.

398 The azimuthal anisotropy found at periods of 44 s and larger could be due

399 to the LPO of olivine in relation to Juan de Fuca slab rollback. The change  
400 in fast direction seen in the northern portion of the region at 85 s and 102 s,  
401 where phase velocities appear faster than average, could be the signature of  
402 a locally modified flow field around the edges of the slab. Conversely, the  
403 roughly homogenous E-W fast directions found at longer periods (28 s to  
404 102 s) are consistent with asthenospheric flow-induced LPO of olivine. The  
405 direction of asthenospheric flow may be driven by Juan de Fuca / Gorda slab  
406 rollback, but is also possibly due to eastward-driven flow from the Pacific  
407 asthenosphere. The change in fast directions seen in the northern portion  
408 of the region, where phase velocities appear faster than average, could be  
409 the signature of a locally modified flow field around the southern edge of the  
410 slab.

411 Because the mantle lithosphere is very thin, it is difficult at this stage  
412 to determine whether the semi-circular fast direction signal is located in the  
413 crust or the mantle part of the lithosphere. We observe, however, correla-  
414 tions between the anisotropy signal and some geological features, which may  
415 indicate a crustal origin for at least part of the shear-wave splitting signal  
416 observed in the region (Savage and Sheehan, 2000; West et al., 2009), as dis-  
417 cussed in section 6.3. Note, however, that given the current lateral resolution  
418 of our models, we cannot tell whether this pattern extends to asthenospheric  
419 depths. Further, we estimated that the strength of the anisotropy found  
420 at short periods (about 3%) would produce roughly 0.4 s of splitting time,  
421 which is about 30% of the total splitting times observed by West et al.  
422 (2009). It therefore suggests that a lithospheric source alone cannot com-  
423 pletely account for the observed regional shear-wave splitting observations,

424 which implies sublithospheric fabric in the region.

### 425 *6.3. The fabric of the Great Basin crust*

426 In this section we explore the relationship between our models and the  
427 tectonics of the Great Basin region. Recently, Wernicke et al. (2008) pro-  
428 posed that the Great Basin is underlain by a crustal megadetachment. The  
429 proposed detachment zones are located where the mantle lid is very thin (see  
430 their Figure 11), which could correspond to channels where asthenospheric  
431 material flows around a region of thicker lithosphere. This could cause basal  
432 tractions at the base of the lithosphere, which could be transmitted to the  
433 crust and generate fabric within the crust and mantle lithosphere. In this  
434 scenario, the flow channel would be located around the central Nevada zone  
435 of lower phase velocity and null azimuthal anisotropy, following the fast direc-  
436 tion of propagation modeled with surface waves. While our models are not of  
437 sufficient resolution to confirm the details of the megadetachment hypothesis,  
438 our results are broadly consistent with this model.

439 An alternative interpretation of the short period anisotropy signal is that  
440 it reflects regional crustal deformation. For instance, in the eastern part of the  
441 study region, the modeled fast direction is oriented north-south, which is also  
442 the general direction of the mountain ranges and north-south trending nor-  
443 mal faults in the area. This region of extension may induce shape-preferred  
444 orientation of crustal cracks (Savage, 1999), which would be orthogonal to the  
445 direction of extension, and would therefore generate  $\sim$  N-S fast directions.  
446 Near the Nevada-California border the fast direction of our 16 s and 18 s  
447 period phase velocity maps is approximately NW-SE, parallel to the East-  
448 ern California Shear Zone/Walker Lane fault system, which accommodates

449 at least 20% of the motion between the North American and Pacific plates  
450 (Dokka and Travis, 1990). The Eastern California Shear Zone represents the  
451 major zone of transitional deformation between the strike-slip plate bound-  
452 ary to the west and the extensional Great Basin zone to the east, which may  
453 generate a shear-driven crustal fabric consistent with our results.

454 The reduced anisotropy in the central Great Basin is more enigmatic.  
455 One possible cause of this reduced zone is that previous crustal cracks asso-  
456 ciate with extension have closed due to more recent compression (or at least  
457 lack of extension) in the central Great Basin as documented by Hammond  
458 and Thatcher (2004). One possible cause of this reduction in extension is  
459 the presence of a lithospheric drip, as suggested by West et al. (2009), which  
460 may cause localized crustal compression (Holt et al., manuscript in prepara-  
461 tion). Crustal compression could lead to a deeper Moho, consistent with the  
462 isotropic part of our phase velocity maps, as discussed in section 6.1.

## 463 **7. Conclusions**

464 We present azimuthally anisotropic phase velocity maps obtained from  
465 fundamental mode Rayleigh-wave measurements made between periods of  
466 16 s and 102 s, which sample structure in the  $\sim 20$  to 200 km depth range.  
467 Our results demonstrate the presence of azimuthal anisotropy over most  
468 depths of the crust and uppermost mantle, suggesting deformation that ex-  
469 tends to significant depth beneath the Great Basin, and constitute the first  
470 depths constraints on the origin of the SKS splitting pattern found in the  
471 region (Savage and Sheehan, 2000; West et al., 2009).

472 We find evidence for a semi-circular fast propagation direction for Rayleigh-

473 waves at short periods (16 s and 18 s), which are sensitive to crustal depths,  
474 around a region of locally reduced phase velocity. This reduction in phase  
475 velocity can be explained by the presence of a locally thick crust, in agree-  
476 ment with crustal receiver function studies (Ozalaybey et al., 1997; Crotwel  
477 and Owens, 2005). While our short period azimuthal anisotropy signal is  
478 similar to the local SKS splitting signal, it can only explain about 30 % of  
479 the total splitting times, implying that the origin of the shear-wave splitting  
480 is complex and must be partly due to asthenospheric fabric development. At  
481 periods of 28 s and higher, which are mostly sensitive to the lower mantle  
482 lithosphere and upper asthenosphere, our azimuthal anisotropy signal is more  
483 laterally uniform with a fast  $\sim$ E-W direction, which we interpret in terms  
484 of present mantle deformation, possibly related to slab rollback.

485 These results shed new light on the different hypotheses that were pre-  
486 viously proposed to explain the semi-circular SKS splitting observations in  
487 the western US. As argued by West et al. (2009), we rule out the possibility  
488 of an upwelling as proposed by Savage and Sheehan (2000), because of the  
489 paucity of young volcanism, and the presence of a heat flow low as well as  
490 a cylindrical fast velocity anomaly beneath the study region. The idea of  
491 toroidal mantle flow around a slab (Zandt and Humphreys, 2008) is more  
492 difficult to reconcile with our short periods azimuthal anisotropy maps: this  
493 model argues in favor of asthenospheric mantle deformation, and it is not  
494 clear how it would generate a semi-circular azimuthal anisotropy pattern in  
495 the crust and/or in the mantle lithosphere. The West et al. (2009) litho-  
496 spheric drip model, however, is not incompatible with our findings. In that  
497 model, the lithosphere is dripping down due to a gravitational instability,

498 and the azimuthal anisotropy-low is due to a rapid, local shift from hori-  
499 zontal to vertical flow. The locally thick crust associated with a reduction  
500 in phase velocity in central Nevada could be a result of vertical extensional  
501 forces due to strong mantle downwelling, which locally draws crust down  
502 with it. The azimuthal anisotropy signal detected in our 16 s and 18 s phase  
503 velocity maps could be interpreted in terms of asthenospheric flow channels  
504 creating basal traction at the base of the lithosphere, which is transmitted to  
505 the crust. Another hypothesis relates the anisotropy signal to crustal defor-  
506 mation, such as the presence of the Eastern California Shear Zone and the  
507 north-south trending mountain ranges and normal faults in the eastern part  
508 of the study region. This cannot explain, however, the total amplitude of the  
509 shear-wave splitting signal and requires an additional mechanism to account  
510 for the remaining  $\sim 70\%$  of the signal.

## 511 **8. Acknowledgements**

512 C.B. wishes to thank Sergei Lebedev and Frederic Deschamps for sharing  
513 their codes, Linda Warren for kindly shared her scripts in the early stage of  
514 the project, and Paul Davis for reviewing the paper before submission. This  
515 research was partially funded by NSF grants EAR-0548288 (MJF EarthScope  
516 CAREER grant).

## 517 **References**

518 Becker, T., Kellogg, J., Ekström, G., O’Connell, R., 2003. Comparison of  
519 azimuthal seismic anisotropy from surface waves and finite strain from  
520 global mantle-circulation models. *Geophys. J. Int.* 155, 696–714.

- 521 Becker, T. W., Schulte-Pelkum, V., Blackman, D. K., Kellogg, J. B.,  
522 O'Connell, R. J., 2006. Mantle flow under the western United States from  
523 shear wave splitting. *Earth Planet. Sci. Lett.* 247, 235–251.
- 524 Beghoul, N., Barazangi, M., 1990. Azimuthal anisotropy of velocity in the  
525 mantle lid beneath the Basin and Range province. *Nature* 348 (6301), 536–  
526 538.
- 527 Ben-Ismaïl, W., Mainprice, D., 1998. An olivine fabric database: an overview  
528 of upper mantle fabrics and seismic anisotropy. *Tectonophysics* 296, 145–  
529 157.
- 530 Bensen, G. D., Ritzwoller, M. H., Shapiro, N. M., 2008. Broadband ambient  
531 noise surface wave tomography across the United States. *J. Geophys. Res.-*  
532 *Solid Earth* 113 (B5).
- 533 Burdick, L., Helmberger, D., 1978. Upper mantle P velocity structure of  
534 western United-States. *J. Geophys. Res.* 83 (B4), 1699–1712.
- 535 Burdick, S., Li, C., Martynov, V., Cox, T., Eakins, J., Mulder, T., Astiz,  
536 L., Vernon, F. L., Pavlis, G. L., van der Hilst, R. D., 2008. Upper mantle  
537 heterogeneity beneath north america from travel time tomography with  
538 global and usarray transportable array data. *Seism. Res. Lett.* 79 (3), 384–  
539 392.
- 540 Catchings, R., Mooney, W., 1991. Basin and Range crustal and upper mantle  
541 structure, northwest to central Nevada. *J. Geophys. Res.-Solid Earth and*  
542 *Planets* 96 (B4), 6247–6267.

- 543 Crampin, S., Chesnokov, E., Hipkin, R., 1984. Seismic anisotropy: the state  
544 of the art. *Geophys. J. R. A. S.* 76 (1), 1–16.
- 545 Crotwell, H., Owens, T., 2005. Automated receiver function processing.  
546 *Seism. Res. Lett.* 76, 702–708.
- 547 Das, T., Nolet, G., 1998. Crustal thickness map of the western United States  
548 by partitioned waveform inversion. *J. Geophys. Res.* 103 (B12), 30,021–  
549 30,038.
- 550 Deschamps, F., Lebedev, S., Meier, T., Trampert, J., 2008a. Azimuthal  
551 anisotropy of rayleigh-wave phase velocities in the east-central United  
552 States. *Geophys. J. Int.* 173 (3), 827–843.
- 553 Deschamps, F., Lebedev, S., Meier, T., Trampert, J., 2008b. Stratified seis-  
554 mic anisotropy reveals past and present deformation beneath the east-  
555 central United States. *Earth Planet. Sci. Lett.* 274, 489–498.
- 556 Dokka, R., Travis, C., 1990. Role of the Eastern California Shear Zone in  
557 accomodating pacific-north american plate motion. *Geophys. Res. Lett.*  
558 17 (9), 1323–1326.
- 559 Dziewonski, A., Bloch, S., Landisman, M., 1969. A technique for the analysis  
560 of transient seismic signals. *BSSA* 59 (1), 427–444.
- 561 Grand, S., Helmberger, D., 1984. Upper mantle shear structure of North  
562 America. *Geophys. J. R. A. S.* 76 (2), 399–438.
- 563 Hammond, W., Thatcher, W., 2004. Contemporary tectonic deformation of  
564 the basin and range province, western united states: 10 years of observa-

- 565 tion with the global positioning system. *J. Geophys. Res.-Solid Earth* 109,  
566 B08403.
- 567 Hearn, T., 1996. Anisotropic  $P_n$  tomography in the western United States.  
568 *J. Geophys. Res.* 101 (B4), 8403–8414.
- 569 Herrmann, R., 1987. Computer programs in seismology. Tech. rep., St. Louis  
570 University, St. Louis, Missouri.
- 571 Holtzman, B., Kohlstedt, D., Zimmerman, M., Heidelbach, F., Hiraga, T.,  
572 Hustoft, J., 2003. Melt segregation and strain partitioning: Implications  
573 for seismic anisotropy and mantle flow. *Science* 301, 1227–1230.
- 574 Jung, H., Karato, S., 2001. Water-induced fabric transitions in olivine. *Sci-*  
575 *ence* 293, 1460–1463.
- 576 Karato, S., Toriumi, M., 1989. Seismic anisotropy; mechanisms and tectonic  
577 implications. pp. 393–422.
- 578 Kennett, B., Engdahl, E., Buland, R., 1995. Constraints on seismic velocities  
579 in the earth from traveltimes. *Geophys. J. Int.* 122, 108–124.
- 580 Knopoff, L., 1972. Observation and inversion of surface-wave dispersion.  
581 *Tectonophysics* 13 (1-4), 497–519.
- 582 Landisman, M., Usami, T., Sato, Y., Masse, R., 1970. Contributions of the-  
583 oretical seismograms to study of modes, rays, and earth. *Reviews of Geo-*  
584 *physics and Space Physics* 8 (3), 533–589.

- 585 Lebedev, S., van der Hilst, R. D., 2008. Global upper-mantle tomography  
586 with the automated multimode inversion of surface and S-wave forms. *Geo-*  
587 *phys. J. Int.* 173 (2), 505–518.
- 588 Lerch, D. W., Glen, J. M. G., Ponce, D. A., Miller, E. L., Colgan, J. P.,  
589 2007. Crustal structure of the northwestern Basin and Range province and  
590 its transition to unextended volcanic plateaus. *Geochemistry Geophysics*  
591 *Geosystems* 8, Q02011.
- 592 Marone, F., Romanowicz, B., 2007. The depth distribution of azimuthal  
593 anisotropy in the continental upper mantle. *nature* 447, 198–203.
- 594 Meier, T., Dietrich, K., Stockhert, B., Harjes, H., 2004. One-dimensional  
595 models of shear wave velocity for the eastern Mediterranean obtained from  
596 the inversion of Rayleigh wave phase velocities and tectonic implications.  
597 *Geophys. J. Int.* 156, 45–58.
- 598 Mitchell, B., Helmberger, D., 1973. Shear velocities at the base of the mantle  
599 from observations of S and ScS. *J. Geophys. Res.* 78, 6009–6020.
- 600 Nettles, M., Dziewonski, A. M., 2008. Radially anisotropic shear velocity  
601 structure of the upper mantle globally and beneath North America. *J.*  
602 *Geophys. Res.-Solid Earth* 113.
- 603 Nicolas, A., Christensen, N., Fuchs, K., Froidevaux, C., 1987. Composi-  
604 tion, Structure and Dynamics of the Lithosphere–Asthenosphere System.  
605 Vol. 16. American Geophysical Union, Washington, DC, Ch. Formation of  
606 anisotropy in upper mantle peridotites: A review, pp. 111–123.

- 607 Ozalaybey, S., Savage, M., Sheehan, A., Louie, J., Brune, J., 1997. Shear-  
608 wave velocity structure in the northern basin and range province from the  
609 combined analysis of receiver functions and surface waves. *BSSA* 87 (1),  
610 183–199.
- 611 Paige, C., Saunders, M., 1982. LSQR - an algorithm for sparse linear-equations  
612 and sparse least-squares. *Acm T Math Software* 8 (1), 43–71.
- 613 Pollitz, F. F., 2008. Observations and interpretation of fundamental mode  
614 rayleigh wavefields recorded by the transportable array (usarray). *Journal*  
615 *of Geophysical Research* 113 (B10).
- 616 Priestley, K., Orcutt, J., Brune, J., 1980. Higher mode surface waves and  
617 the structure of the Great Basin of Nevada and western Utah. *J. Geophys.*  
618 *Res.* 85, 7166–7174.
- 619 Ribe, N., 1989. Seismic anisotropy and mantle flow. *J. Geophys. Res.* 94,  
620 4213–4223.
- 621 Roth, J., Fouch, M., James, D., Carlson, R., 2008. Three-dimensional seismic  
622 velocity structure of the northwestern United States. *Geophys. Res. Lett.*  
623 35.
- 624 Sass, J. H., Lachenbruch, A., Jr., S. P. G., Morgan, P., Priest, S. S., Jr., T.  
625 H. M., Munroe, R. J., 1994. Thermal regime of the southern basin and  
626 range province: 1. heat flow data from arizona and the mojave desert of  
627 california and nevada. *J. Geophys. Res.* 99 (B11), 22,093–22,119.

- 628 Sato, Y., 1955. Analysis of dispersed surface waves by means of Fourier trans-  
629 form I. Bull. Earthquake Res. Tokyo Univ. 33, 33–50.
- 630 Savage, M., 1999. Seismic anisotropy and mantle deformation: What have  
631 we learned from shear wave splitting? Rev. Geophys. 37 (1), 65–106.
- 632 Savage, M., Sheehan, A., 2000. Seismic anisotropy and mantle flow from the  
633 Great Basin to the Great Plains, western United States. J. Geophys. Res.  
634 105 (B6), 13,715–13,734.
- 635 Sheehan, A., Jones, C., Savage, M., Ozalaybey, S., Schneider, J., 1997. Con-  
636 trasting lithospheric structure between the Colorado Plateau and Great  
637 Basin: Initial results from Colorado Plateau - Great Basin PASSCAL ex-  
638 periment. Geophys. Res. Lett. 24 (21), 2609–2612.
- 639 Sieminski, A., L ev eque, J., Debayle, E., 2004. Can finite-frequency effects  
640 be accounted for in ray theory surface wave tomography? Geophys. Res.  
641 Lett. 31.
- 642 Sigloch, K., McQuarrie, N., Nolet, G., June 2008. Two-stage subduction his-  
643 tory under North America inferred from multiple-frequency tomography.  
644 Nature Geoscience.
- 645 Silver, P., Holt, W., 2002. The mantle flow field beneath western North  
646 America. Science 295 (5557), 1054–1057.
- 647 Simpson, R., Jachens, R., Blakely, R., 1986. A new isostatic residual gravity  
648 map of the conterminous united states with a discussion on the significance  
649 of isostatic residual anomalies. J. Geophys. Res. 91 (88), 8348–8372.

- 650 Smith, D., Ritzwoller, M., Shapiro, N., 2004. Stratification of anisotropy in  
651 the Pacific upper mantle. *J. Geophys. Res.* 109 (B11).
- 652 Smith, M., Dahlen, F., 1973. The azimuthal dependence of Love and Rayleigh  
653 wave propagation in a slightly anisotropic medium. *J. Geophys. Res.* 78,  
654 3321–3333.
- 655 Trampert, J., 1998. Global seismic tomography: the inverse problem and  
656 beyond. *Inverse Problems* 14 (3), 371–385.
- 657 Trampert, J., Lévêque, J., 1990. Simultaneous iterative reconstruction tech-  
658 nique - physical interpretation based on the generalized least-squares so-  
659 lution. *J. Geophys. Res.-Solid Earth and Planets* 95 (B8), 12553–12559.
- 660 Trampert, J., Spetzler, J., 2006. Surface wave tomography: finite-frequency  
661 effects lost in the null space. *Geophys. J. Int.* 164, 394–400.
- 662 Trampert, J., Woodhouse, J., 2003. Global anisotropic phase velocity maps  
663 for fundamental mode surface waves between 40 and 150 s. *Geophys. J.*  
664 *Int.* 154, 154–165.
- 665 van der Hilst, R., de Hoop, M., 2005. Banana-doughnut kernels and mantle  
666 tomography. *Geophys. J. Int.* 163 (3), 956–961.
- 667 Warren, L., Snoke, J., James, D., 2008. S-wave velocity structure beneath  
668 the High Lava Plains, Oregon, from Rayleigh-wave dispersion inversion.  
669 *Earth Planet. Sci. Lett.* 274, 121–131.
- 670 Wernicke, B., Davis, J., Niemi, N., Luffi, P., Bisnath, S., 2008. Active  
671 megadetachment beneath the western United States. *J. Geophys. Res.* 113.

- 672 West, J., Fouch, M., Roth, J., Elkins-Tanton, L., 2009. Vertical mantle flow  
673 associated with a lithospheric drip beneath the great basin. *Nature Geo-*  
674 *science*.
- 675 Yang, Y., Forsyth, D. W., 2006. Regional tomographic inversion of the am-  
676 plitude and phase of Rayleigh waves with 2-D sensitivity kernels. *Geophys.*  
677 *J. Int.* 166, 1148–1160.
- 678 Yang, Y., Ritzwoller, M. H., Lin, F., Moschetti, M. P., Shapiro, N. M., 2008.  
679 Structure of the crust and uppermost mantle beneath the western united  
680 states revealed by ambient noise and earthquake tomography. *J. Geophys.*  
681 *Res.* 113 (B12).
- 682 Zandt, G., Humphreys, E., 2008. Toroidal mantle flow through the western  
683 U.S. slab window. *Geology* 36 (4), 295–298.
- 684 Zandt, G., Myers, S., Wallace, T., 1995. Crust and mantle structure across  
685 the Basin and Range-Colorado plateau boundary at  $37^{\circ}N$  latitude and im-  
686 plications for cenozoic extensional mechanism. *J. Geophys. Res.* 100 (B6),  
687 10,529–10,548.
- 688 Zhou, Y., Dahlen, F., Nolet, G., Laske, G., 2005. Finite-frequency effects in  
689 global surface-wave tomography. *Geophys. J. Int.* 163, 1087–1111.

690 Figure 1: Tectonic setting of the western United States. The white box  
691 indicates the boundary of the study region.

692 Figure 2: Single-station Rayleigh-wave group velocities *vs.* period for the  
693 15 October 2006 Hawaii event. (A) FTAN plot for station M11A (epicentral  
694 distance  $\Delta = 4482$  km) and (B) station O06A ( $\Delta = 4114$  km), which are  
695 separated by 368.4 km. The difference (dbaz) between the backazimuths  
696 of the far station (M11A) to the epicenter and to the near station (O06A)  
697 is 1.2 deg. The x's are computer-picked energy maxima for each period,  
698 and the vertical lines span  $\pm 1$  dB. Contours are placed every 3 dB. The  
699 corresponding waveforms are shown on the sides.

700 Figure 3: Selected events location (black stars), stations (black triangles  
701 on land), and event-station great circle paths (grey). A few of the 28 selected  
702 events have effectively the same location.

703 Figure 4: (A) Phase velocities calculated from the phase of the coherence  
704 of the observed waveforms for the inter-station path between stations M11A  
705 and O06A. The error bar for each phase velocity is based on the coherence of  
706 the two waveforms after the near-station waveform has been time-shifted to  
707 the far-station epicentral distance using the calculated phase velocities. The  
708 solid line is the phase-velocity dispersion curve generated from the velocity  
709 model mTNA. The dotted lines in panels (B) and (C) are for spectral ampli-  
710 tudes and the time-shifted time series of O06A (near station), respectively.

711 The solid lines are for the (unaltered) M11A waveform.

712 Figure 5: Reduced  $\chi^2$ -misfit, as defined in equation 8, as a function of  
713 the trace of the resolution matrix for inversions of phase velocities measured  
714 at 44s period. The solid thick curve was obtained by inverting equation 2  
715 only for the  $0\Psi$  term. Different values of the trace of the resolution ma-  
716 trix were obtained by varying the level of damping applied (lower damping  
717 corresponding to higher values of the trace of  $\mathbf{R}$ ). The dashed grey curve  
718 corresponds to inversions for the  $0\Psi$  and  $2\Psi$  terms and a fixed (moderate)  
719 amount of damping imposed on the  $0\Psi$  term. Changes in the  $2\Psi$  damping  
720 factor provided different values for the trace of  $\mathbf{R}$ . The thin solid line was  
721 obtained by inversions for the  $0\Psi$ ,  $2\Psi$ , and  $4\Psi$  terms, with moderate  $0\Psi$   
722 and  $2\Psi$  smoothing factors kept fixed, and by varying the damping on the  
723  $4\Psi$  terms. The crosses mark our "preferred" models in the  $0\Psi + 2\Psi$  and the  
724  $0\Psi + 2\Psi + 4\Psi$  inversions. With an F-test we determined that the reduction  
725 in misfit between the "preferred" models is significant.

726 Figure 6: Azimuthally anisotropic phase velocity maps between 16 s  
727 and 102 s period. The background colors represent the isotropic ( $0\Psi$ ) part  
728 of equation 2. The black lines show the fast direction of propagation for  
729 Rayleigh waves calculated from the  $2\Psi$  terms of equation 2. The reference  
730 phase velocity, calculated using the reference mTNA model, is given on top  
731 of each each map.

732 Figure 7: Ray coverage obtained between 16 s and 102 s period. The  
733 location of the TA stations is shown by the black triangles. The background  
734 color is the isotropic ( $0\Psi$ ) part of the maps (see Figure 6).

735 Figure 8: Partial derivatives for fundamental-mode Rayleigh wave phase  
736 velocities with respect to  $V_S$  based on velocity model mTNA. They are plot-  
737 ted as a function of depth for the different periods analyzed.

738 Figure 9: Peak and mean amplitudes for the  $2\Psi$  part of the phase velocity  
739 maps obtained at selected periods between 16 s and 102 s

740 Figure 10: Synthetic tests for inversions done at 18 s and 44 s period.  
741 Input models are on the left (A, C, and E) and the outputs are on the  
742 right (B, D, and F). Input model A was created using the results of the real  
743 data inversion at 18 s. The anisotropy of models C and E is identical to  
744 that of model A but the background phase velocity is different. Model C  
745 assumes a uniformly negative phase velocity anomaly and model E assumes  
746 a positive velocity anomaly associated with the anisotropy-low in central  
747 Nevada, similar to what could be expected from a model such as the one  
748 described by West et al. (2009).



Event date	Event time	Location	Latitude	Longitude	Depth (km)	Magnitude
2006-09-10	14:56:07.4	Gulf of Mexico	26.33	-86.58	10	5.6
2006-10-15	17:07:48.4	Hawaii	19.82	-156.03	29	6.7
2006-11-19	18:57:33.7	Central East Pacific Rise	-4.49	-104.75	10	6.2
2006-12-03	20:52:20.6	Guatemala	14.08	-91.24	62.8	5.8 (Mb)
2007-01-31	03:15:55.7	Kermadec Islands	-29.59	-177.93	34.0	6.3
2007-02-04	20:56:58.8	Cuba Region	19.48	-78.30	10.0	5.9
2007-02-24	02:36:22.0	Off Coast of Northern Peru	-6.9	-80.32	23	6.1
2007-04-07	07:09:26.1	Azores Islands Region	37.36	-24.50	8.0	5.9
2007-04-13	05:42:23.0	Guerrero, Mexico	17.3	-100.1	28.80	5.8
2007-04-25	13:34:16.3	Vanatu Islands	-14.29	166.86	55	5.7
2007-05-04	12:06:52.6	North of Ascension Island	-5.52	-14.87	7.0	5.9
2007-05-12	11:31:05.1	Eastern New Guinea Region	-5.52	146.12	43.6	5.3
2007-05-17	19:29:10.2	Kermadec Islands	-30.60	-178.22	40.7	5.6
2007-05-27	18:12:35.0	Tonga Islands Region	-20.05	-174.53	6.8	5.8 (Mb)
2007-06-08	13:32:01.7	Near Coast of Guatemala	13.80	-90.84	47.8	5.4
2007-06-13	19:29:46.0	Near Coast of Guatemala	13.63	-90.73	23	6.5
2007-06-14	13:37:41.5	Southeast of Easter Island	-36.23	-99.96	10.0	5.4
2007-06-14	17:41:05.0	New Britain Region, Papua New Guinea	-5.71	151.61	41.0	5.6
2007-07-03	08:26:00.7	Central Mid-Atlantic Ridge	0.71	-30.24	10.0	5.9
2007-07-06	17:40:54.8	Samoa Islands Region	-16.30	-172.82	10.0	5.1
2007-07-09	06:50:50.7	South of Fuji Islands	-26.29	-178.14	10.0	5.3
2007-08-09	17:25:05.5	Northern Mid-Atlantic Ridge	25.81	-44.99	10.0	5.1
2007-08-12	12:05:26.7	Santa Cruz Islands	-11.35	166.15	42.0	5.7
2007-08-19	01:22:38.2	Near Coast of Peru	-13.54	-76.47	11.00	5.4
2007-08-19	20:11:44.5	Near Coast of Peru	-13.58	-76.38	35.0	5.2
2007-09-01	01:56:49.0	Northern Mid-Atlantic Ridge	27.79	-44.04	10.0	5.0
2007-09-01	19:14:30.4	Gulf of California	25.14	-109.67	9.0	5.9
2007-09-10	01:49:10.5	Near West Coast of Columbia	2.91	-78.15	15.0	6.7

Table 1: Selected events date, time, locations, and magnitudes. Unless otherwise specified, magnitudes are Ms magnitudes reported by the Iris DMC.

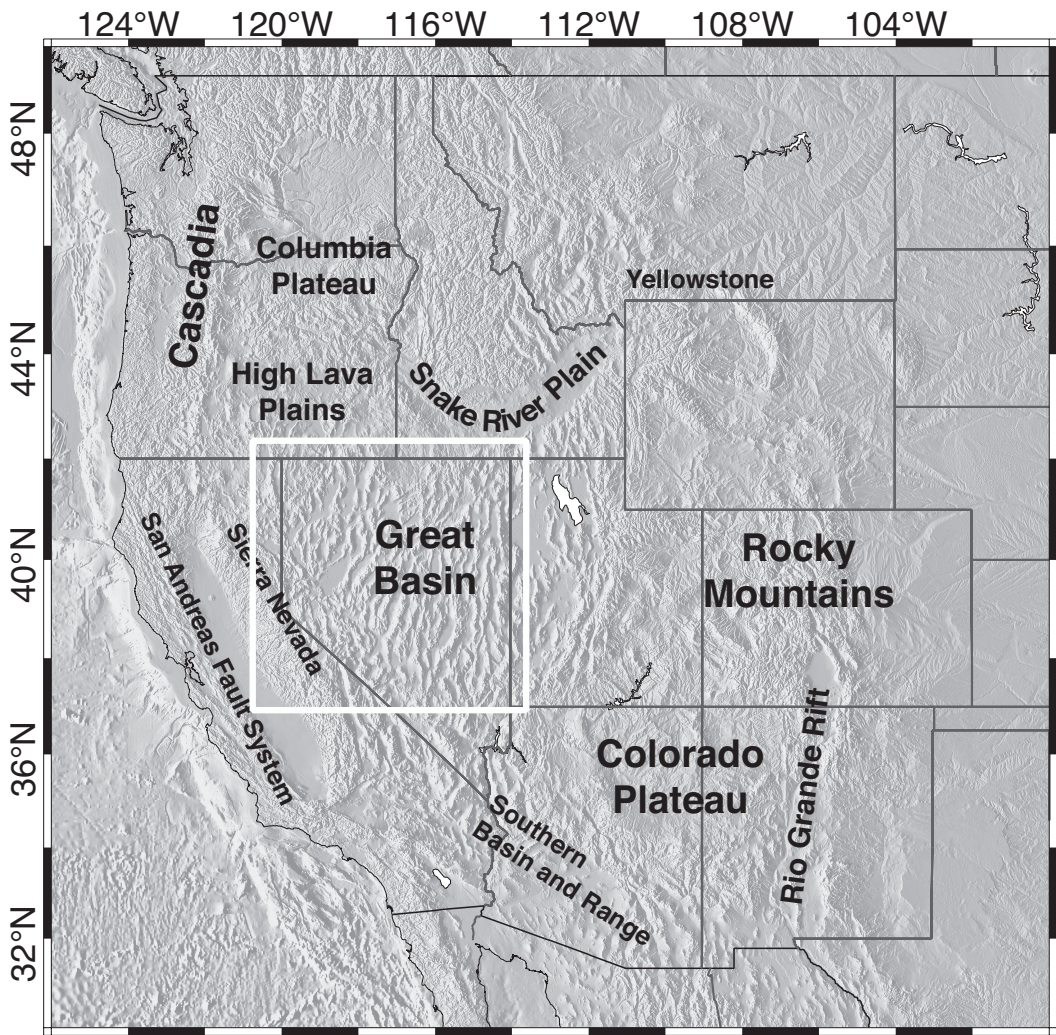


Figure 1:

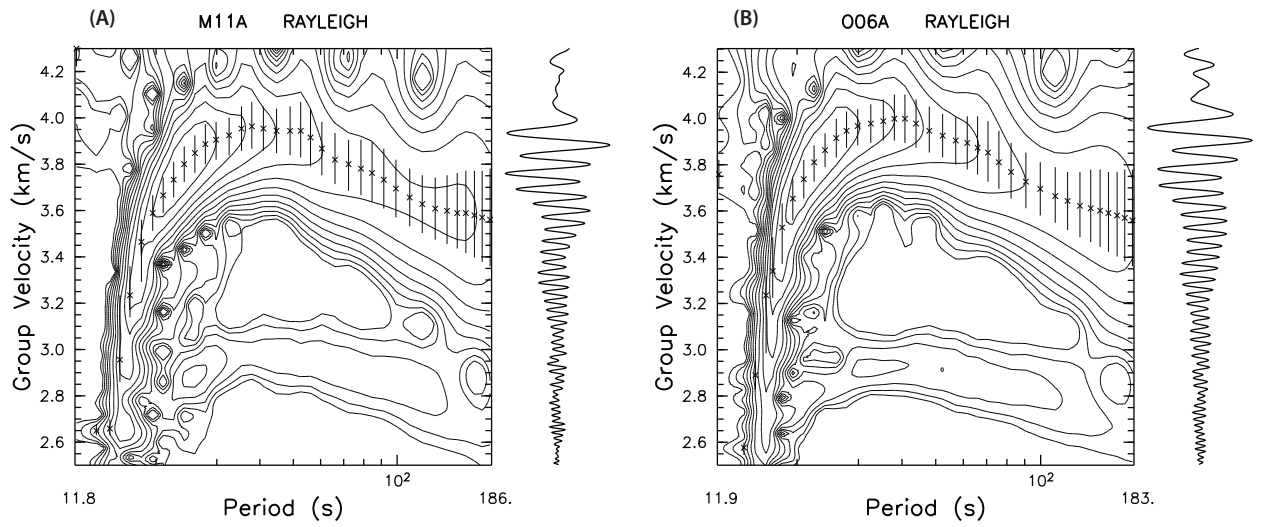


Figure 2:

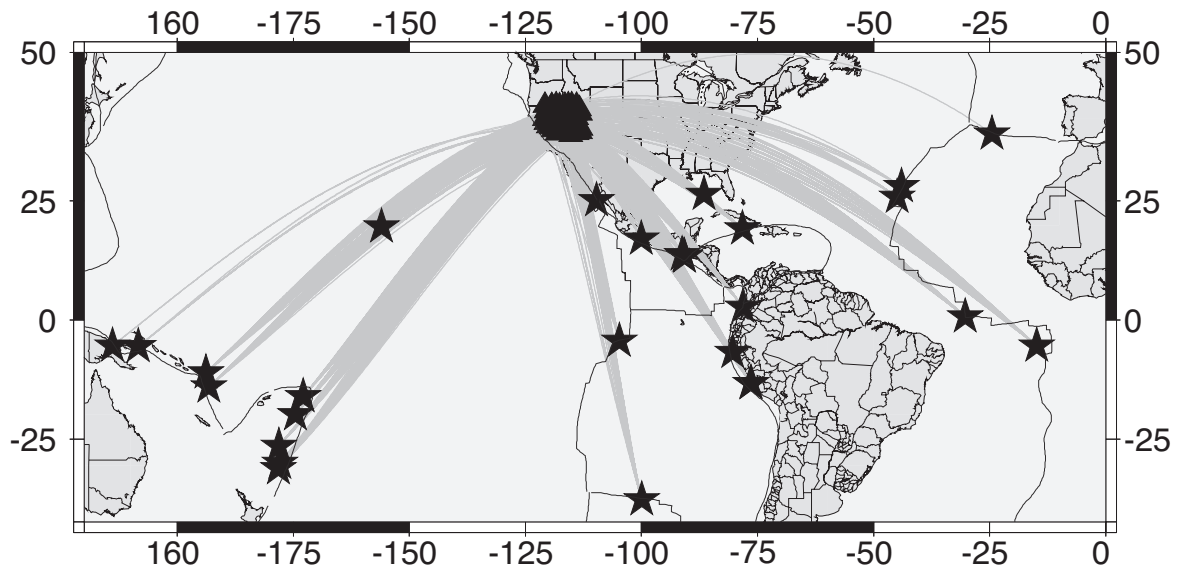


Figure 3:

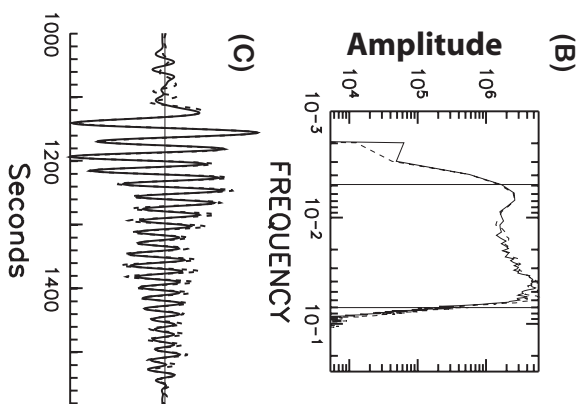
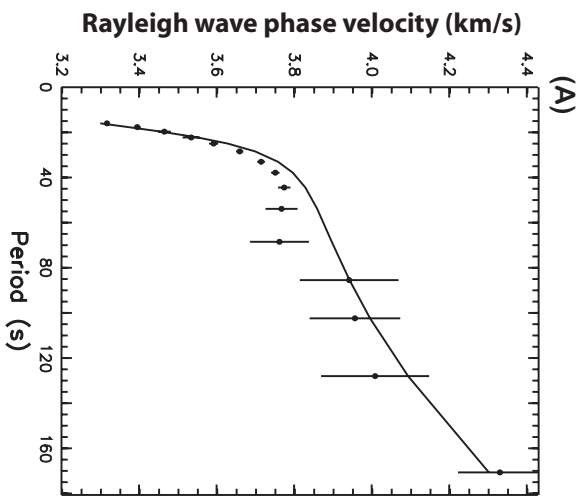


Figure 4:

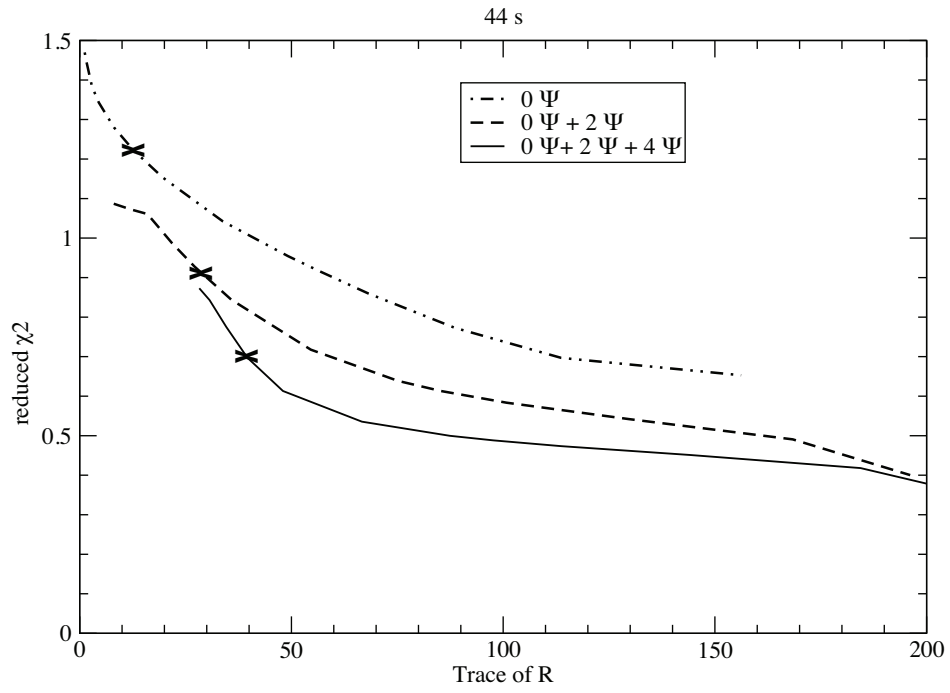


Figure 5:

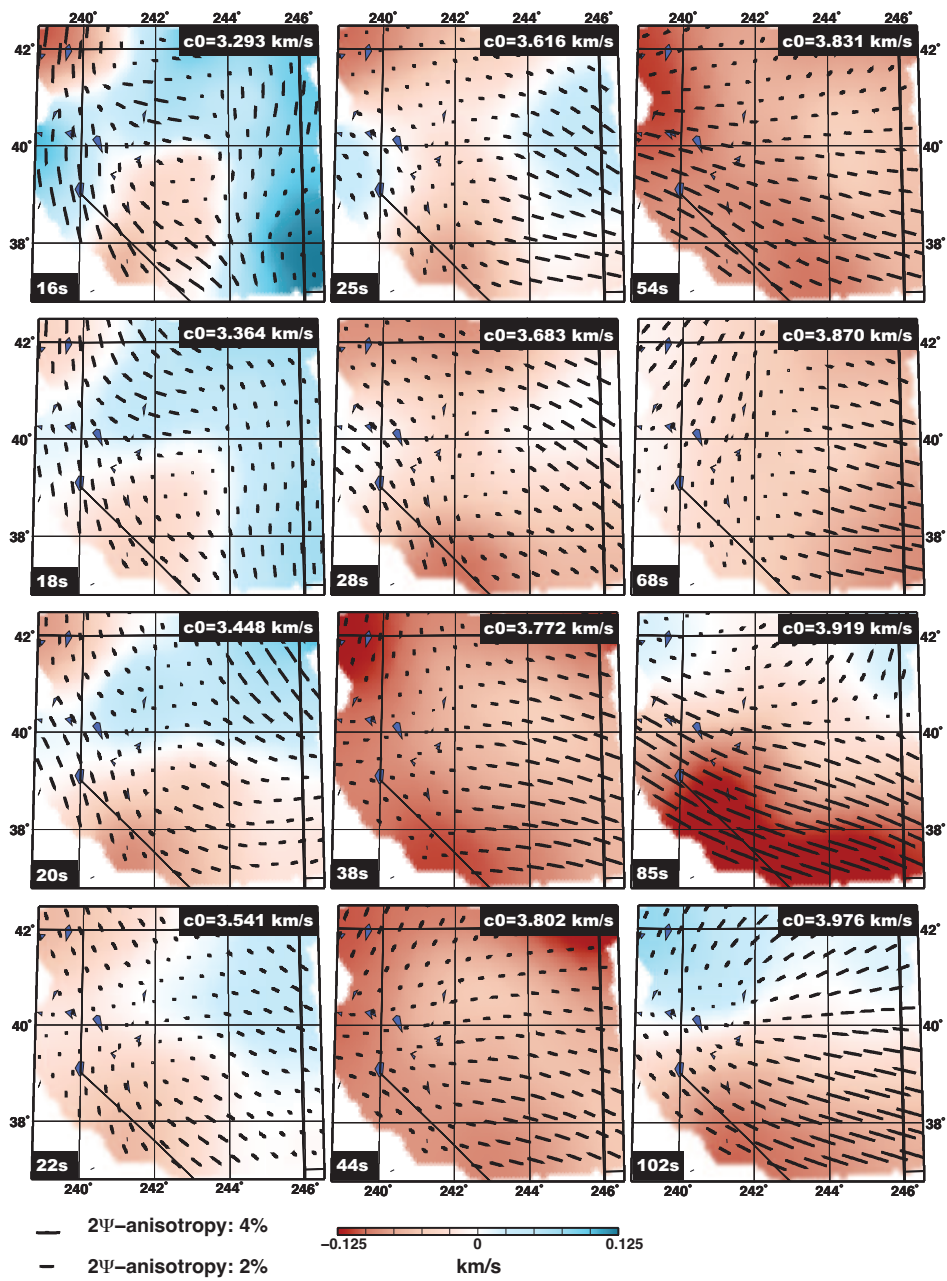


Figure 6:

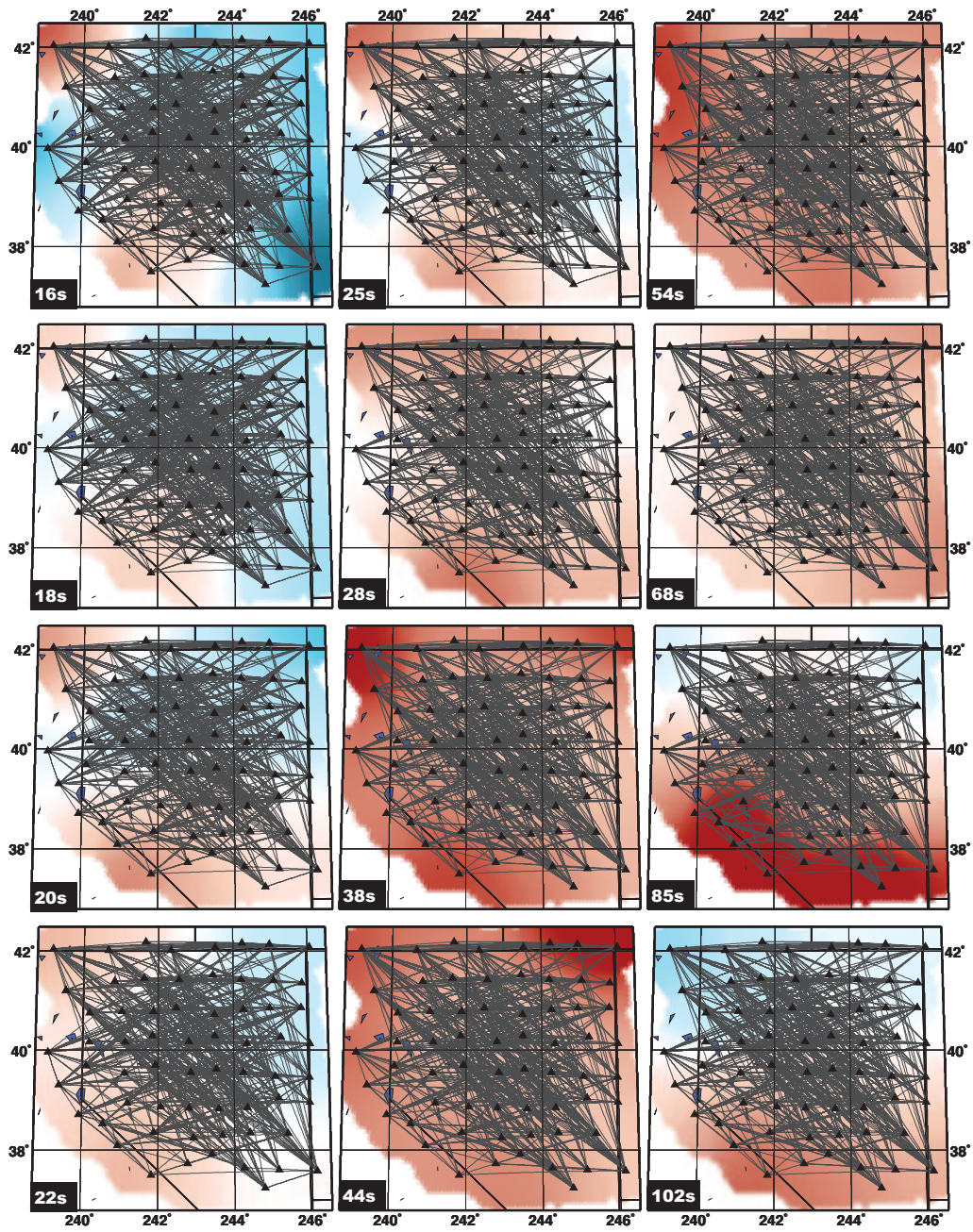


Figure 7:

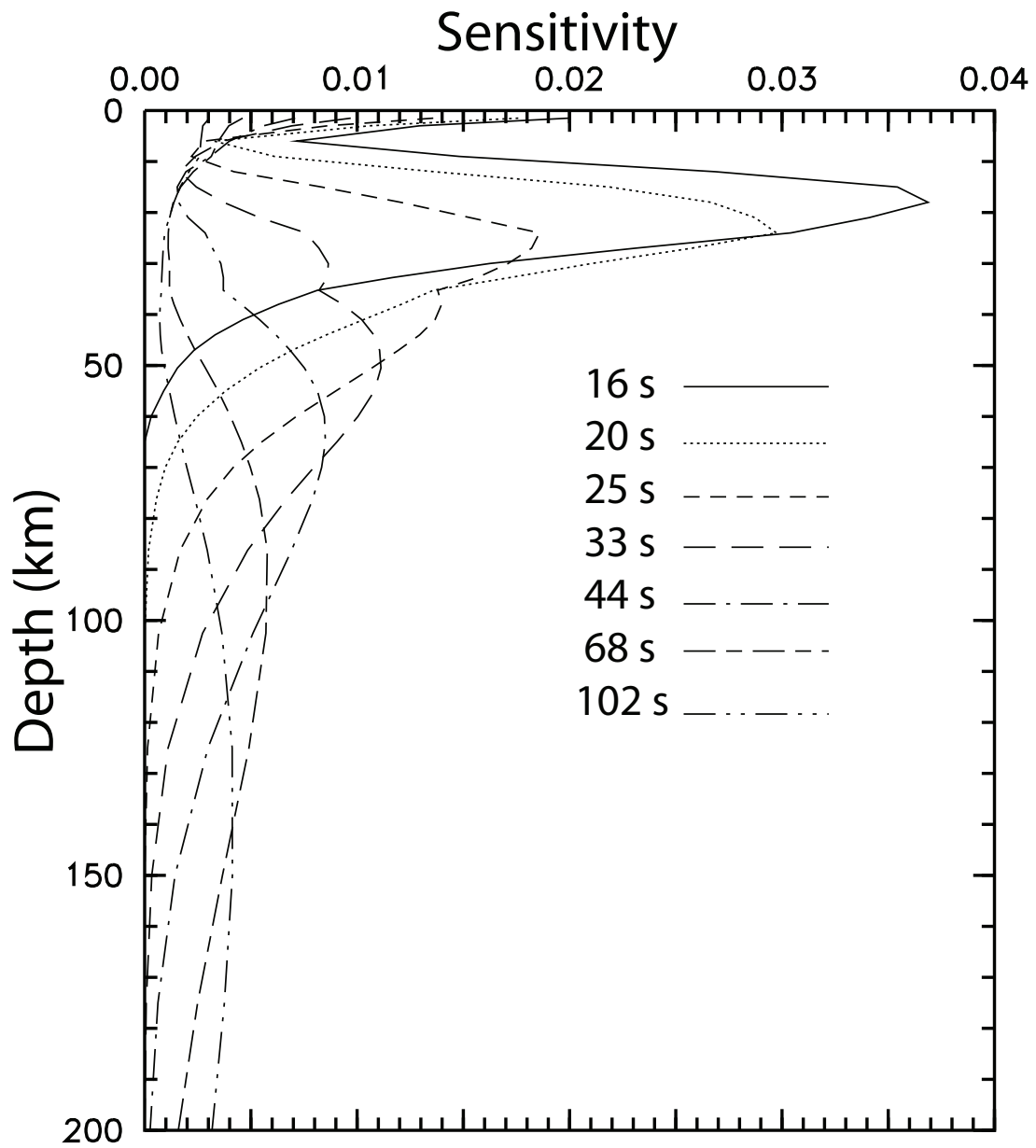


Figure 8:

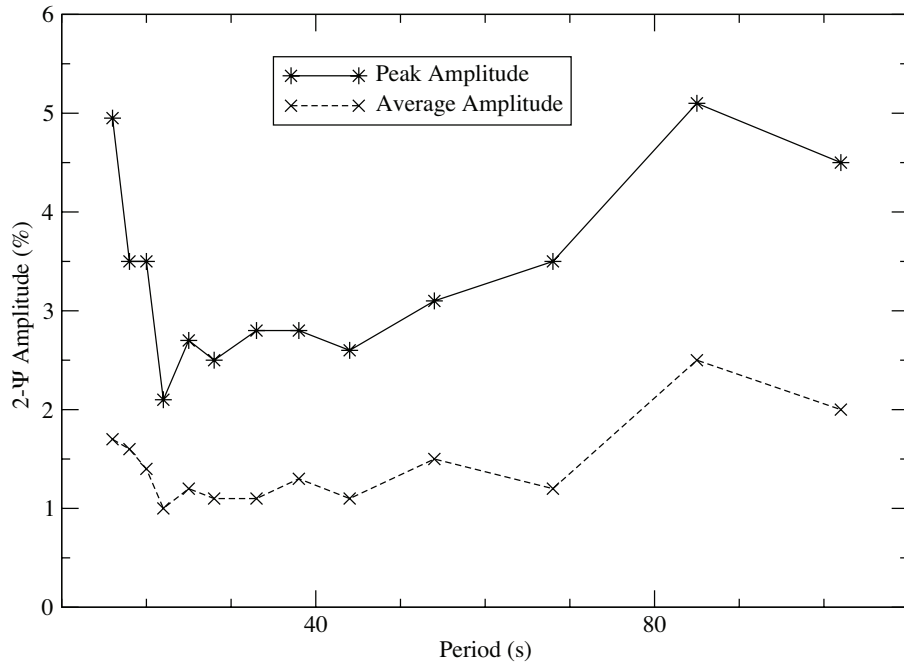


Figure 9:

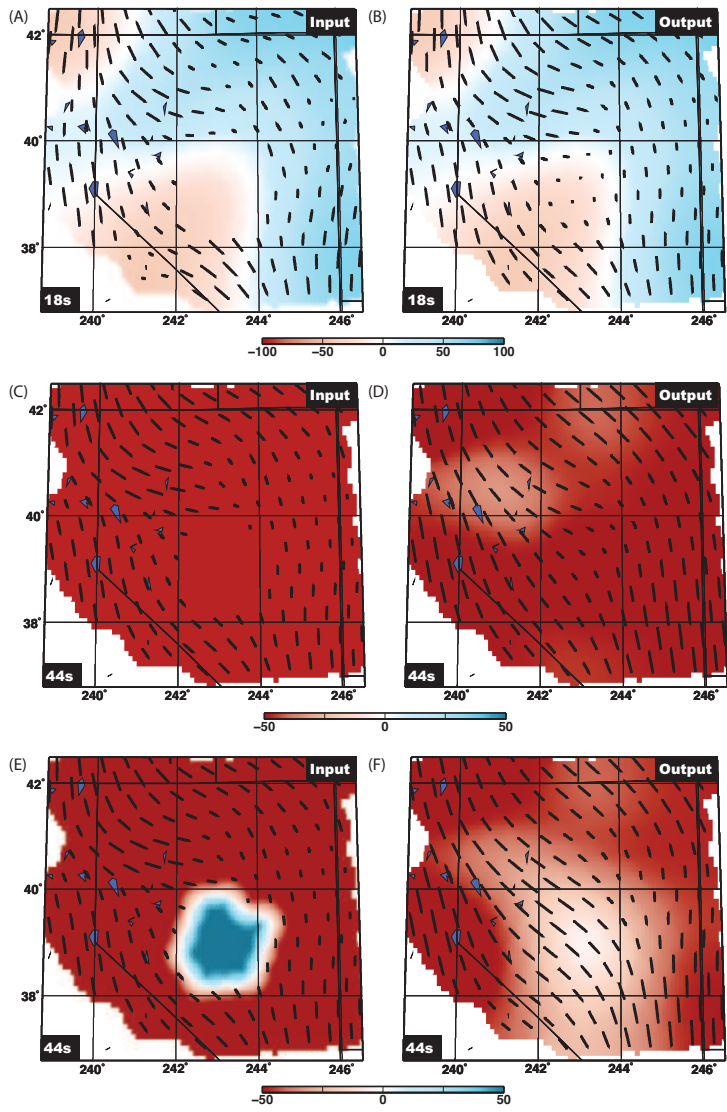
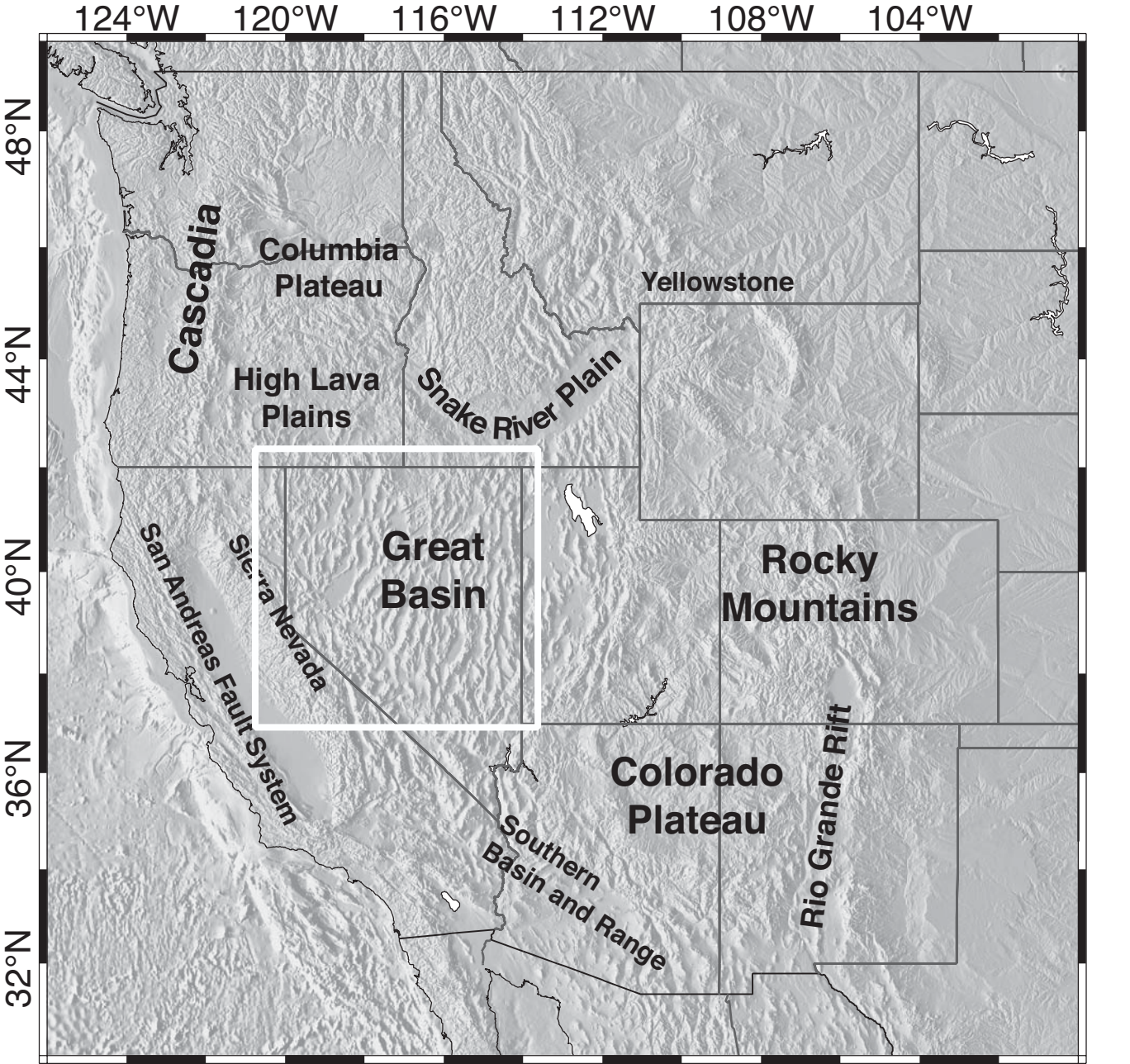
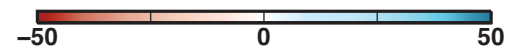
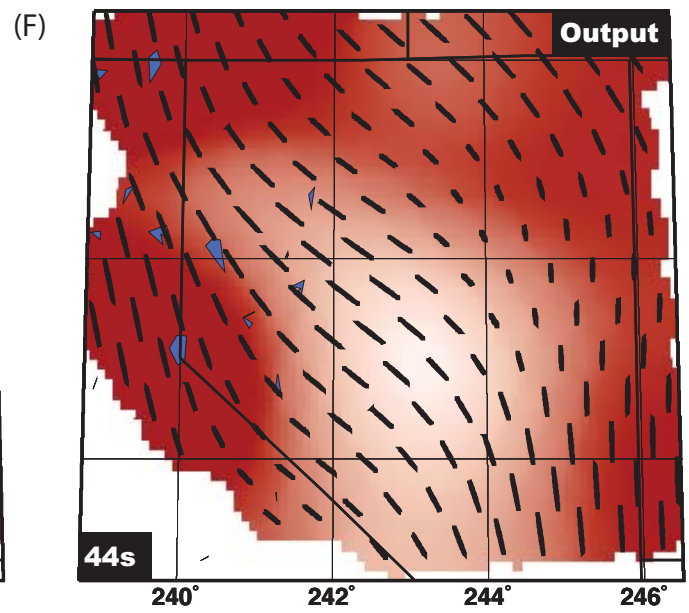
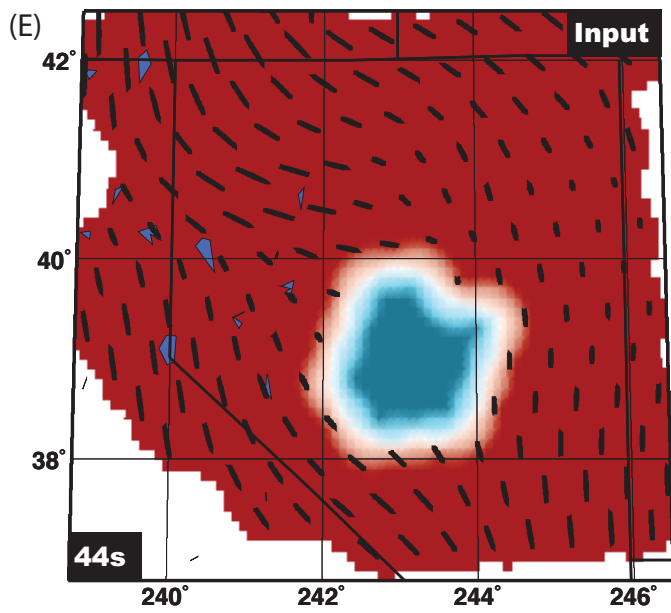
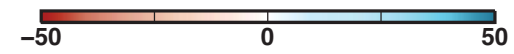
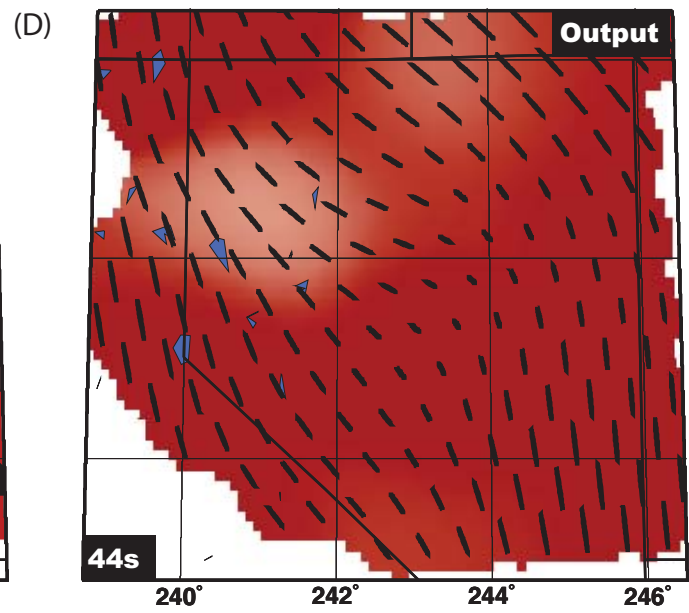
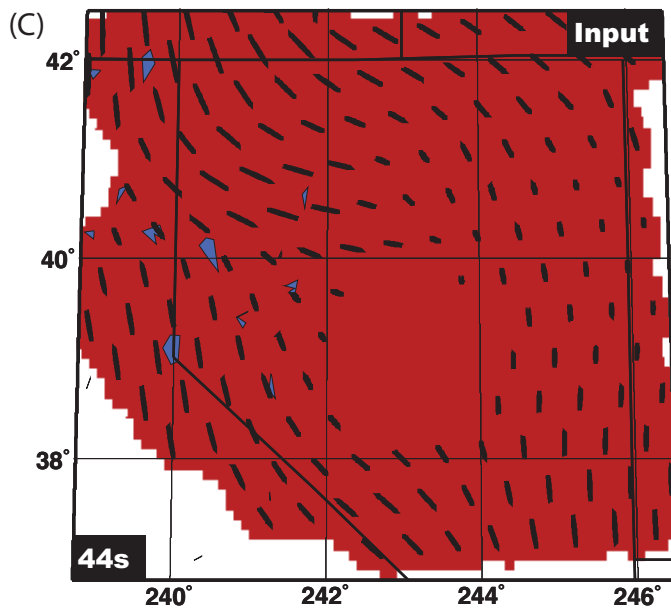
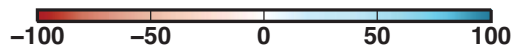
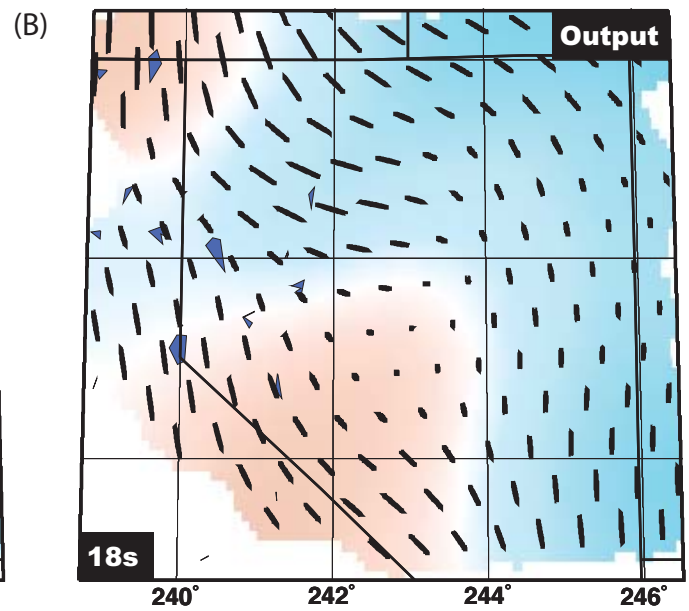
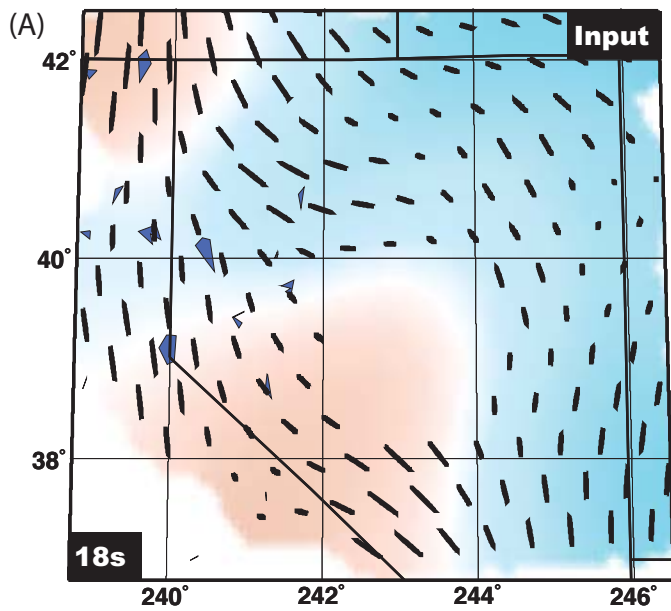
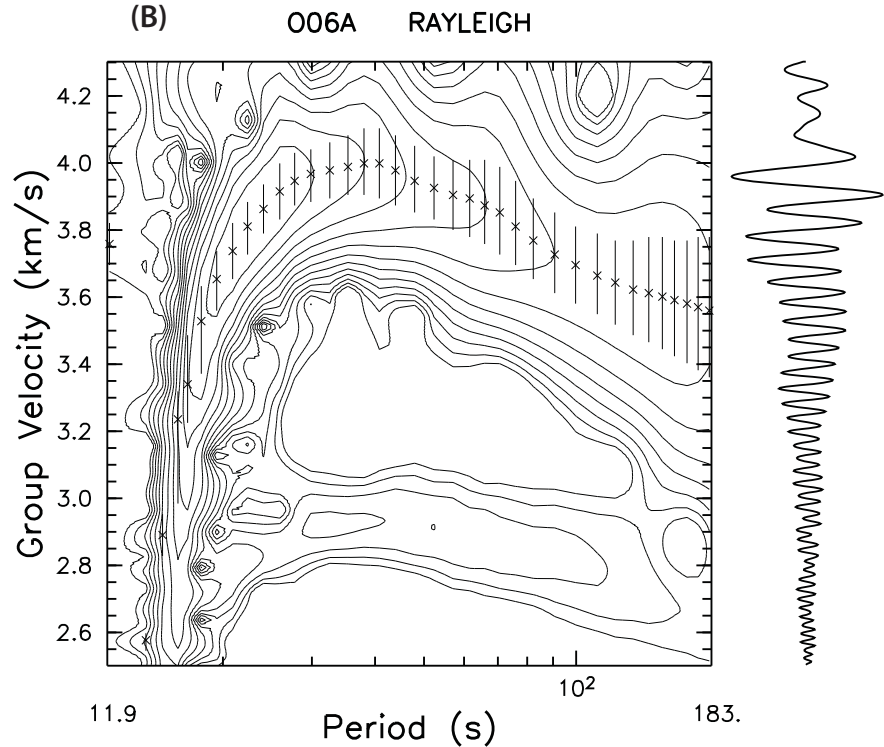
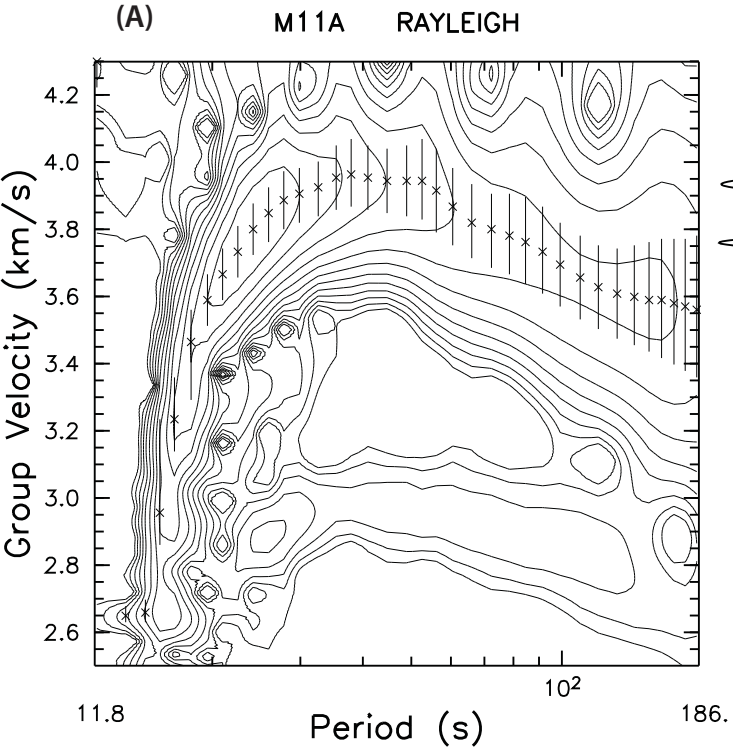
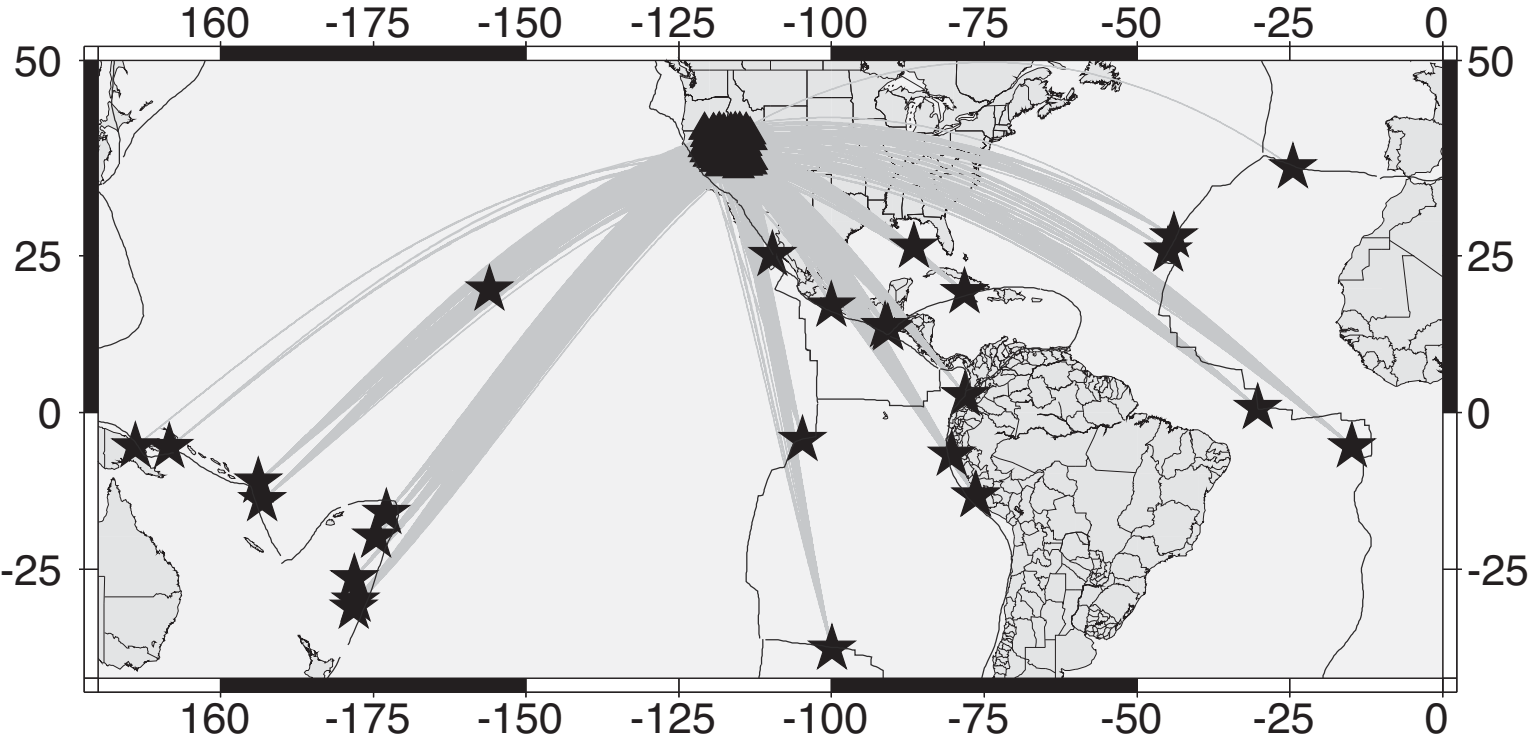


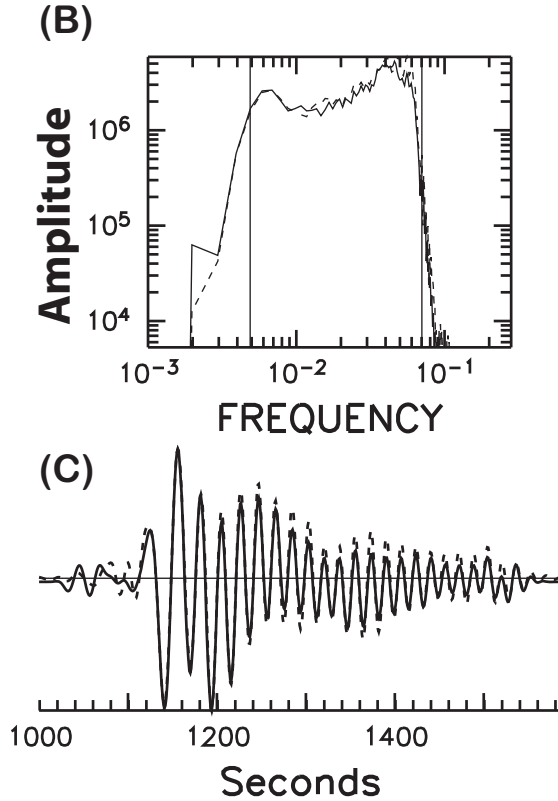
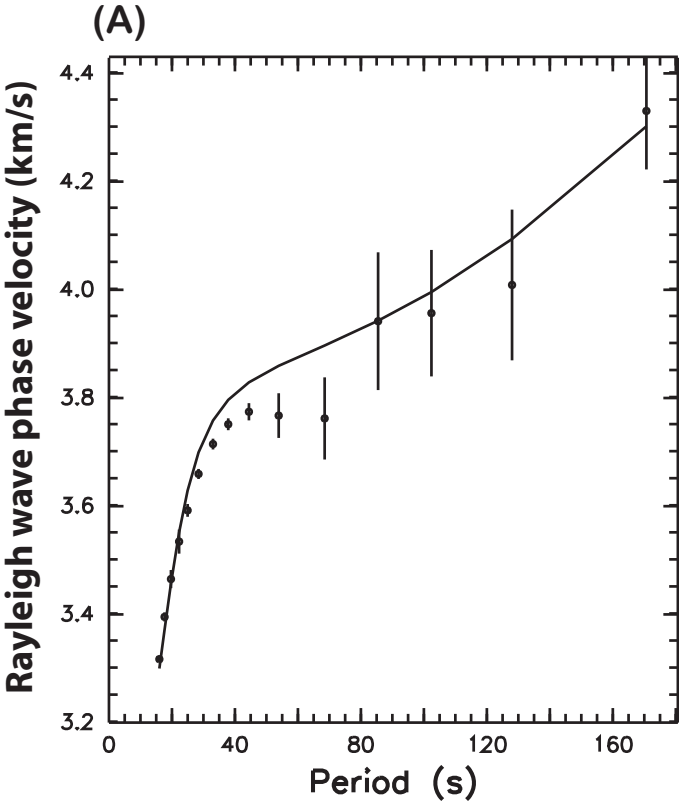
Figure 10:



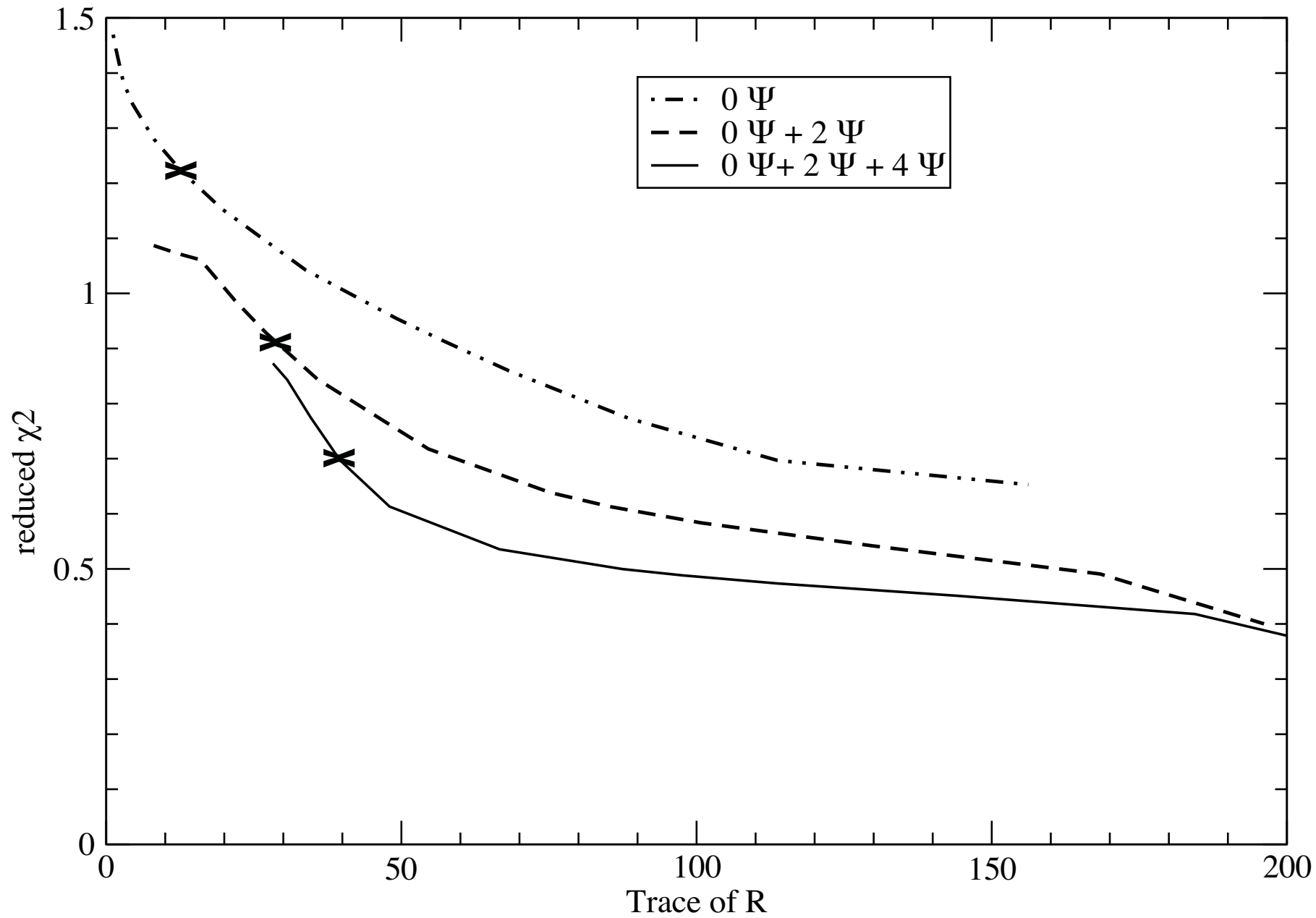


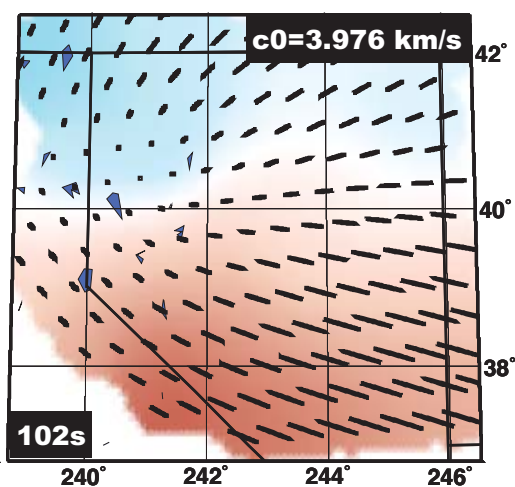
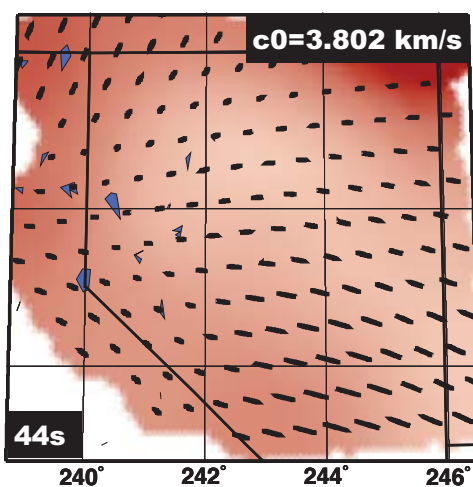
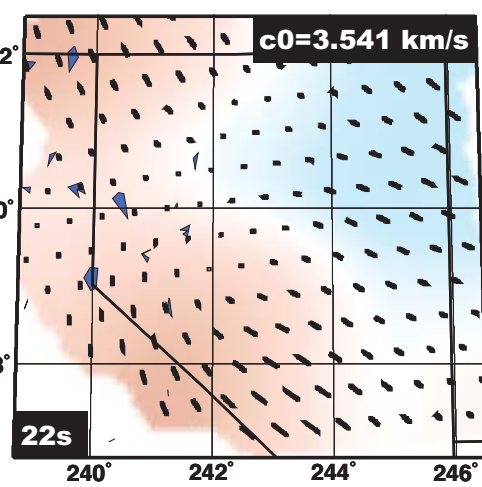
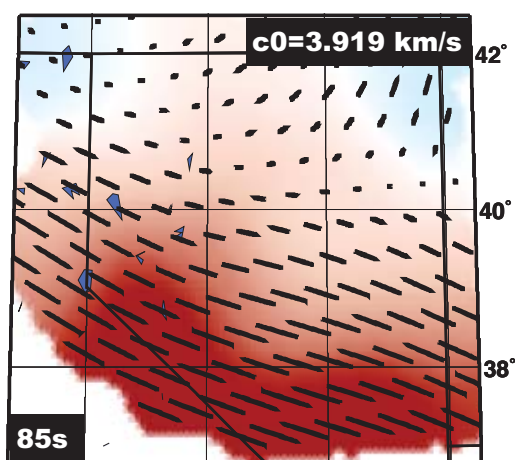
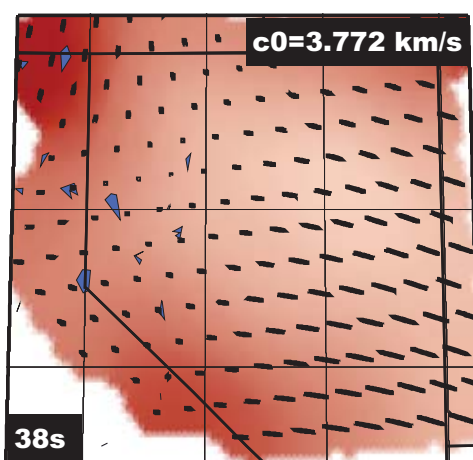
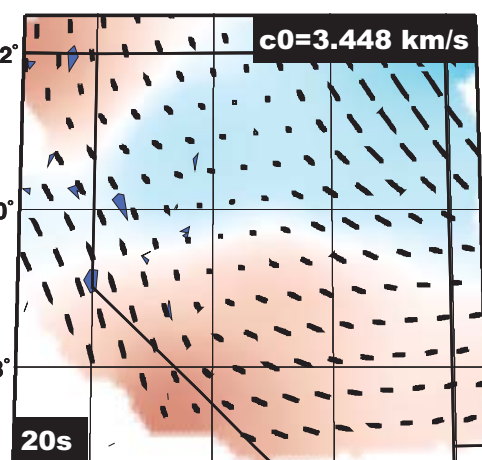
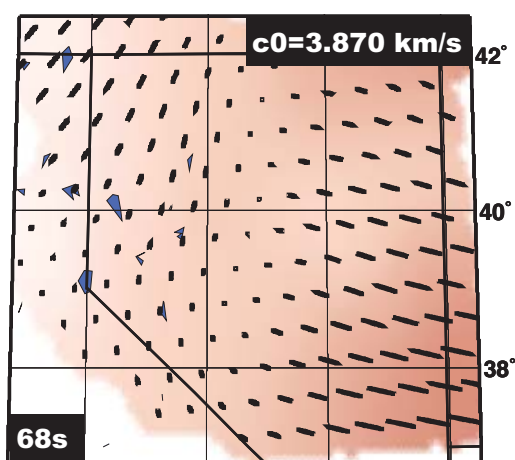
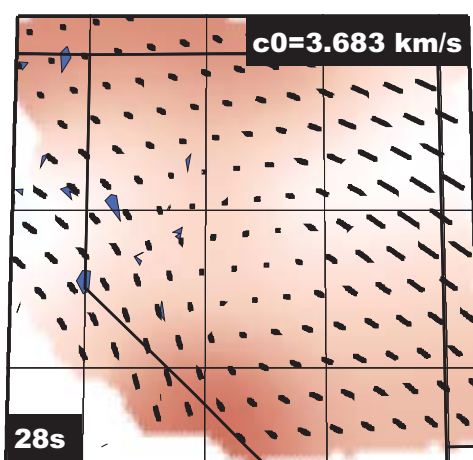
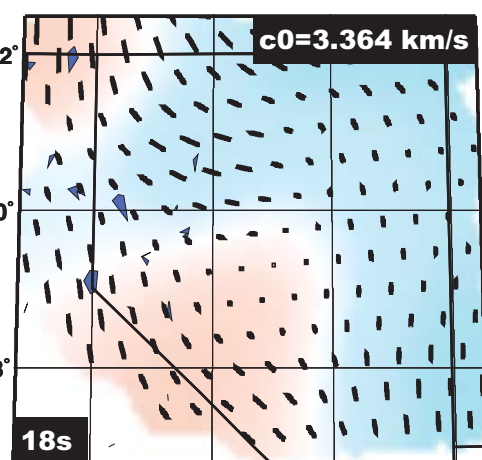
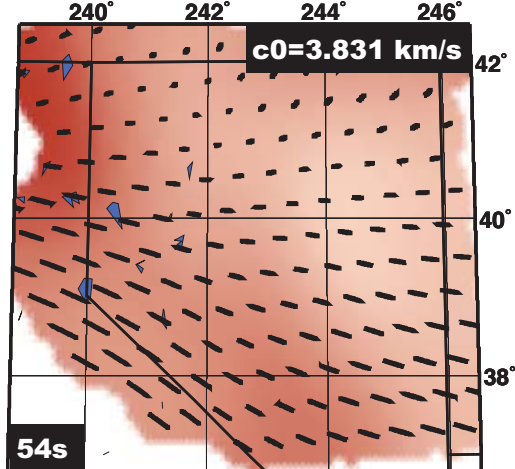
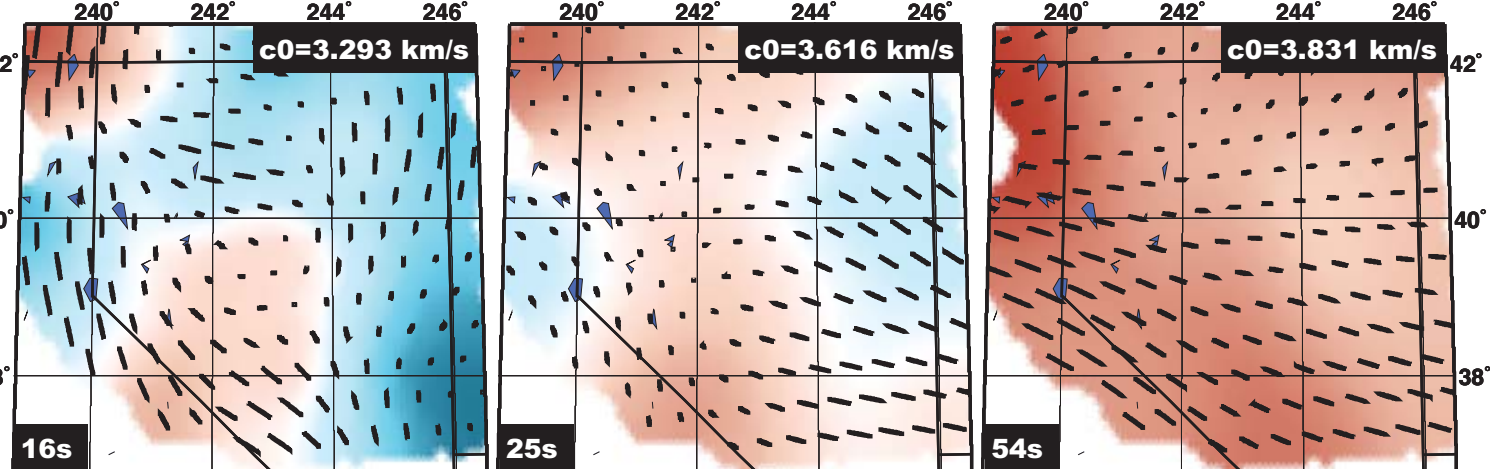






44 s





—  $2\Psi$ -anisotropy: 4%

-  $2\Psi$ -anisotropy: 2%

